Electronic Supplementary Material (ESI) for Energy & Environmental Science

Supplementary Information for

Active MOF water harvester with extraordinary productivity enabled by cooling-enhanced sorption

Yaohui Feng, Lurong Ge, Yao Zhao, Qian Li, Ruzhu Wang, Tianshu Ge

Engineering Research Center of Solar Power & Refrigeration (MOE), Institute of Refrigeration and Cryogenics, Shanghai Jiao Tong University, Shanghai 200240, China

This file includes:

Supplementary Figures S1-S37
Supplementary Tables S1-S10
Supplementary Notes S1-S6

Table of contents:

Supplementary Figures

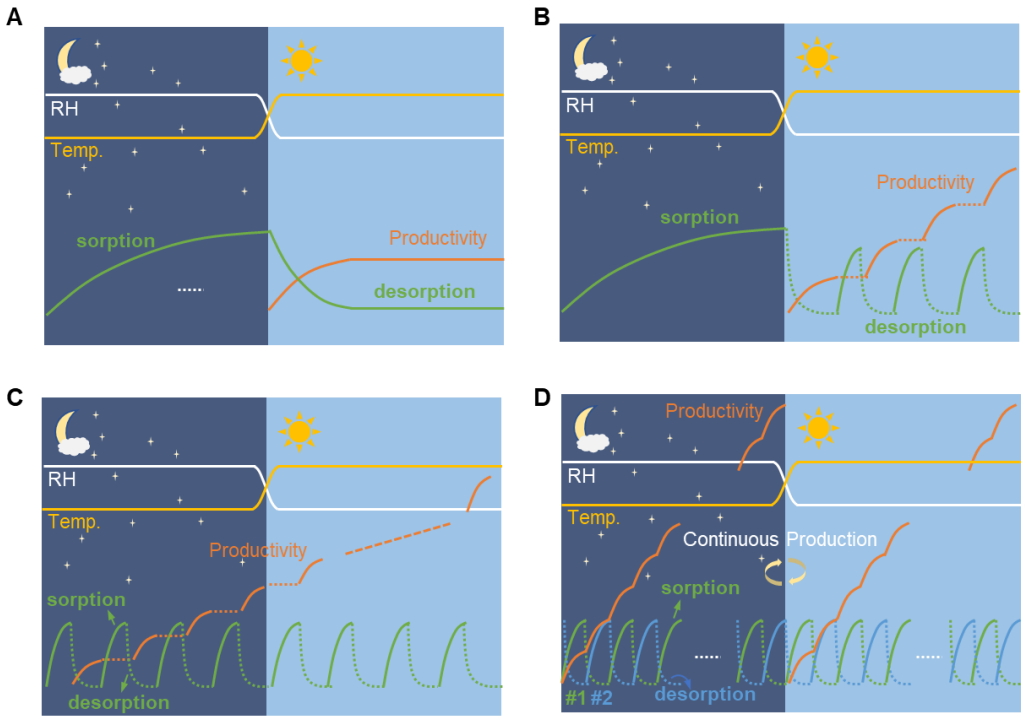

Fig. S1. Operation strategies of different AWH modes. (A) Monocyclic AWH. (B) Sorption at night and multiple sorption-desorption cycles at daytime. (C) Multicyclic AWH at day and night. (D) Continuous multicyclic AWH with two sorbent units.

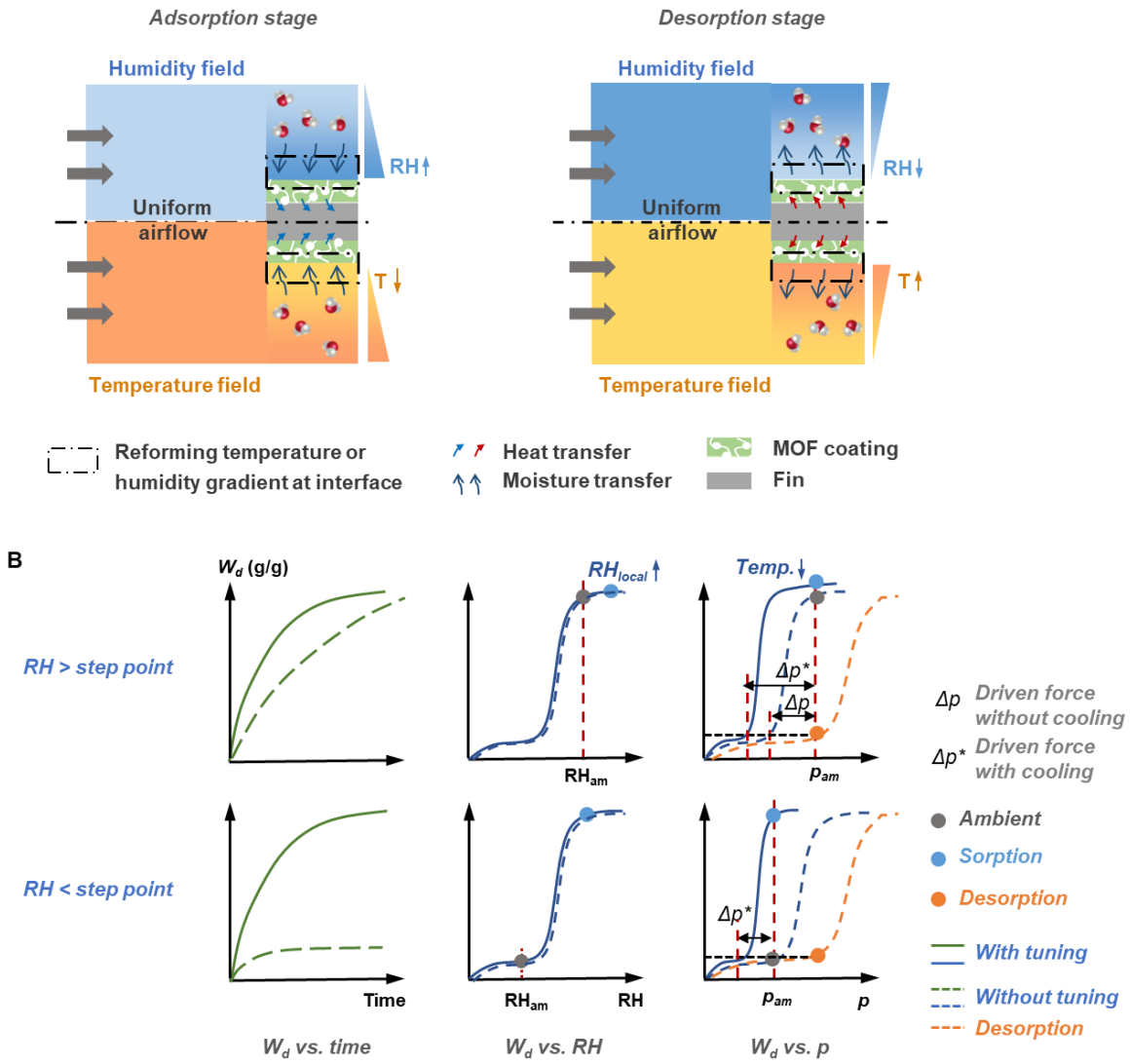

Fig. S2. Heat and moisture transfer of tunable MOF adsorber. (A) Temperature and humidity field of airflow and reforming gradient at the interface between air and sorbent. (B) Tunable dynamics and sorption behaviors when ambient RH is higher or lower than step position of MOF. W_d and p refer to the water sorption capacity of MOF and water vapor pressure, respectively. The local RH means the RH near the sorbent and pore of MOF. Although the isotherm (W_d vs. RH) shows little difference with different temperature, the sorption humidity is not the same as the ambient RH. The tuning process can be obviously identified in the isotherm with vapor pressure due to the constant pressure and different temperature. Δp and Δp* present the driven force of sorption without and with cooling effects, respectively.

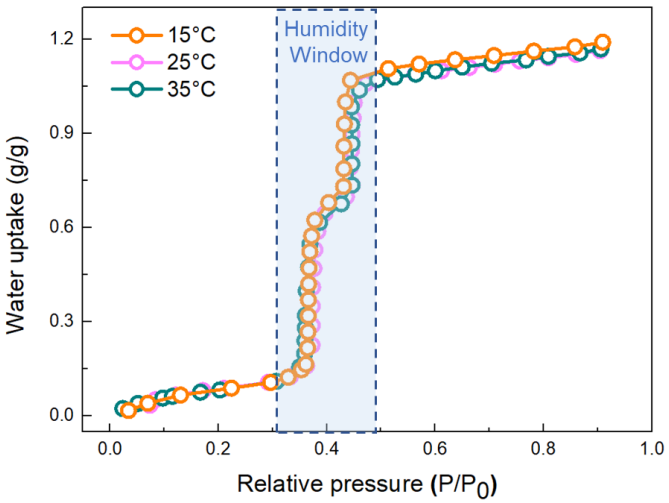

Fig. S3. Water sorption isotherms at different temperature.

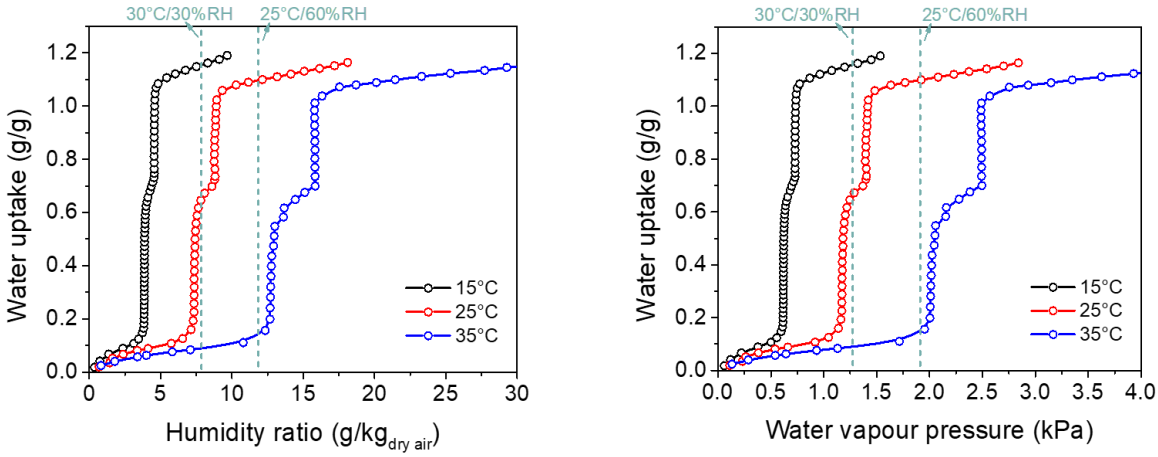

Fig. S4. Water sorption isotherms varied with absolute pressure and humidity

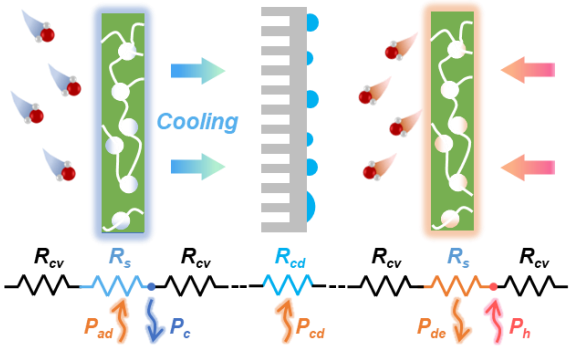

Fig. S5. Basic configurations of cooling-enhanced SAWH and heat transfer resistance network. The R_{cv}, R_s, and R_{cd} refer to the thermal resistance for convection, solid sorbent, and condensation, respectively. P_{ad}, P_c, P_{cd}, P_{de}, and P_h represent the energy for adsorption, cooling, condensation, desorption and heating, respectively. Adsorption and desorption occur with the cooling and heating supply (P_c and P_h), meanwhile, the sorption heat (P_{ad}) can be eliminated by the cooling effect, and extra cooling energy could be recovered to the condenser.

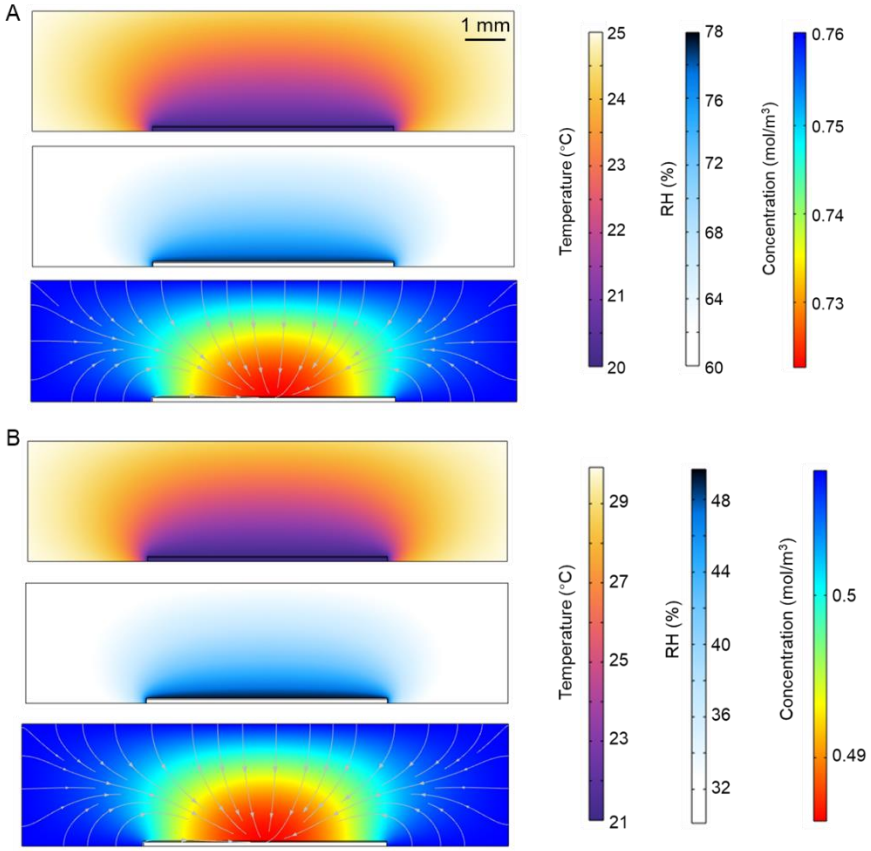

Fig. S6. Temperature, humidity and water vapor concentration fileds induced by cooling effects. (A) Simulated results at 25°C/60%RH with cooling temperature of 20°C. (B) Simulated results at 30°C/30%RH with cooling temperature of 21°C. The simulation was conducted by COMSOL Multiphysics 6.2. The size of aluminum substrate is 60×1mm (W×H), the thickness of sorbent coating is 0.3mm, and the size of air channel is 120×30 mm (W×H).

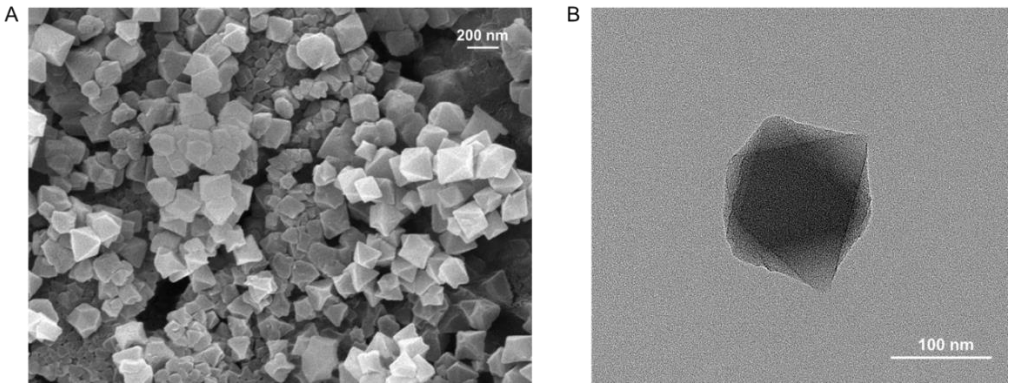

Fig. S7. SEM and TEM of synthesized MOF particle

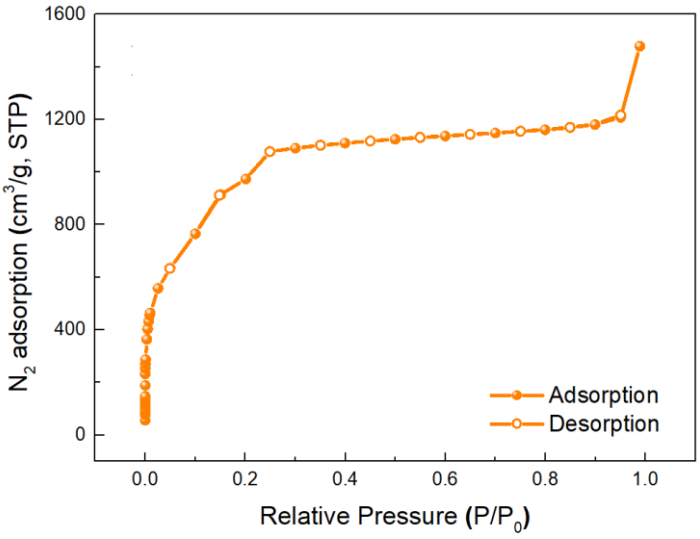

Fig. S8. N_2 isotherms of synthesized MOF particle.

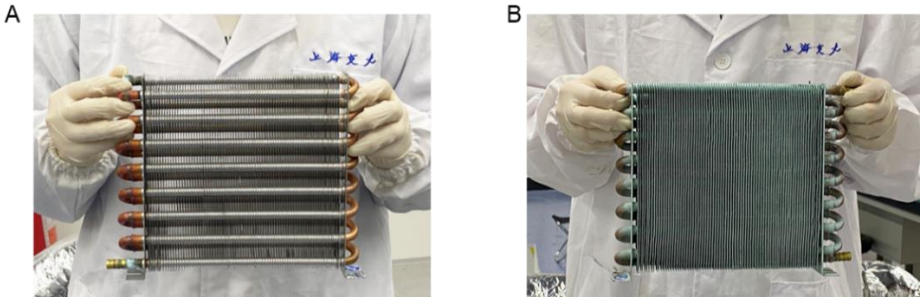

Fig. S9. Bare heat exchanger (A) and MOF adsorber (B).

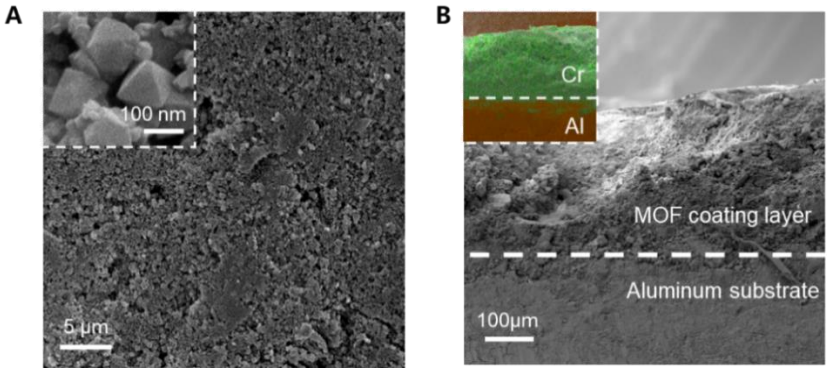

Fig. S10. SEM of MOF coating. (A) Surface SEM, (B) Cross-section SEM

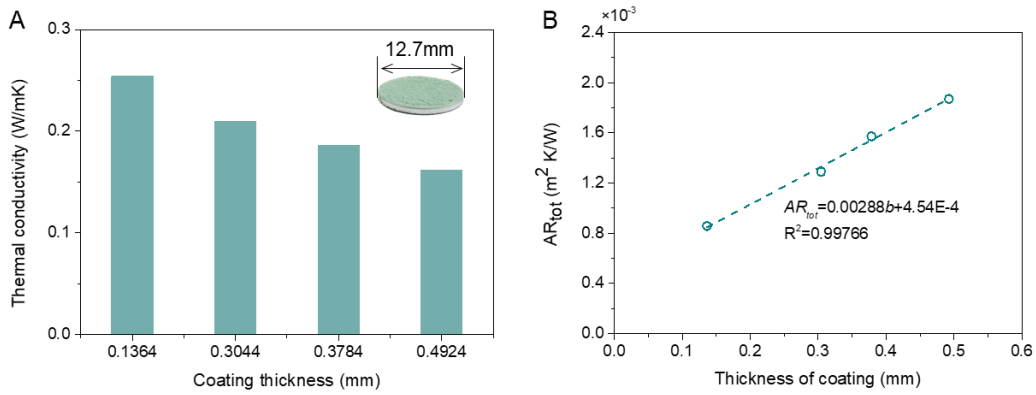

Fig. S11. Thermal analysis of MOF coating layer. (A) Thermal conductivity of MOF coating with different thickness. (B) Relationship between total thermal resistance (solid-side) and thickness of coating. The intercept of fitting line is the sum of thermal resistance of aluminum substrate (4.41×10^{-6} m^2K/W) and contact resistance, indicating that the contact resistance is ca. 4.50×10^{-4} m^2K/W.

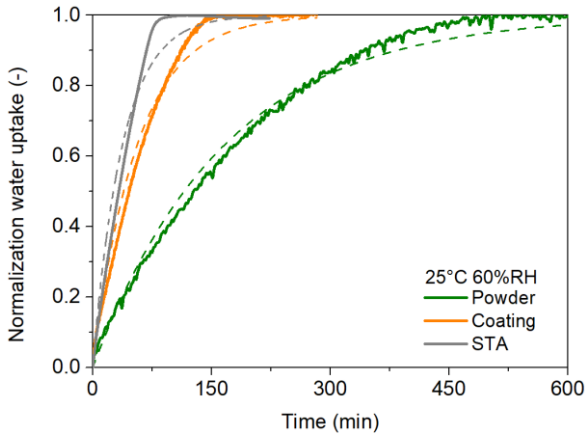

Fig. S12. Normalized dynamic sorption with different MOF form at 25°C/60%RH. The coating and power tests are carried out using the same mass of MOF (~0.305 g), which coated on the aluminum sheet and put in the petri dish with the same area (6×6 cm), respectively. The linear driving force model (LDF, see Note S5) revealed that the kinetics constant of the gram-level powder test in the climate chamber (1.0×10^{-4} s^{-1}) is lower than that in the commercial sorption analyzer (Synchronous Thermal Analyzer, STA) test using 10mg MOF (4.43×10^{-4} s^{-1}), but the coating method will relatively promote the sorption rate (2.96×10^{-4} s^{-1}) owing to the enlarged contact surface with air.

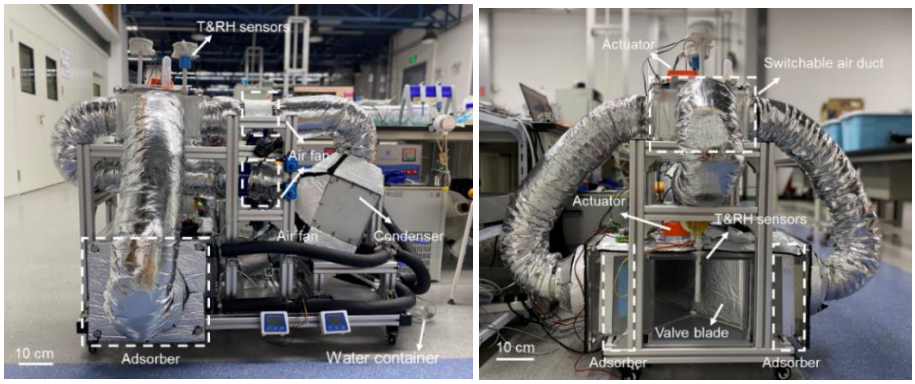

Fig. S13. Side and front view of actual MOF water harvester.

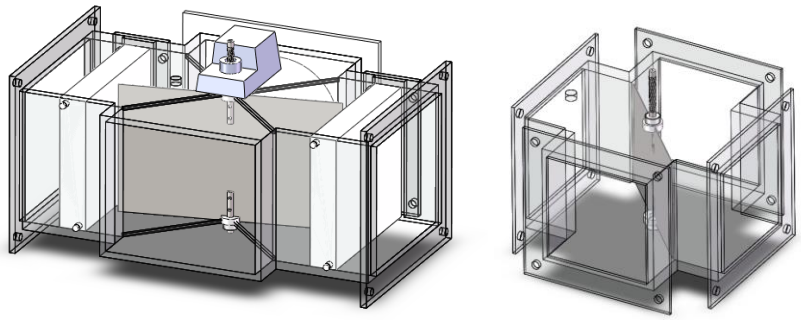

Fig. S14. Switchable air duct with two adsorbers

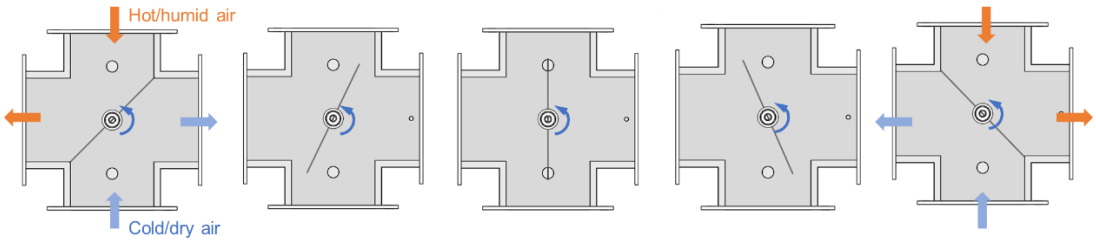

Fig. S15. Evolution of air flow during the switchover. Due to two mixed airflows during the switchover, the switch peak can be observed in the dynamic sorption and desorption curves.

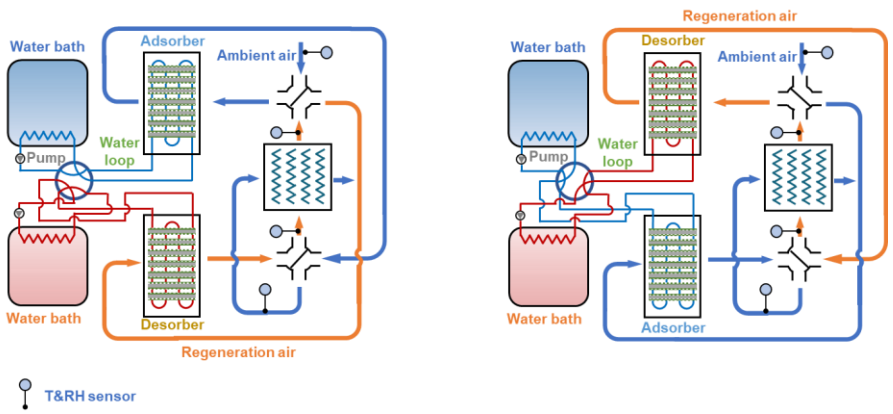

Fig. S16. Test rig of MOF water harvester with controlled temperature.

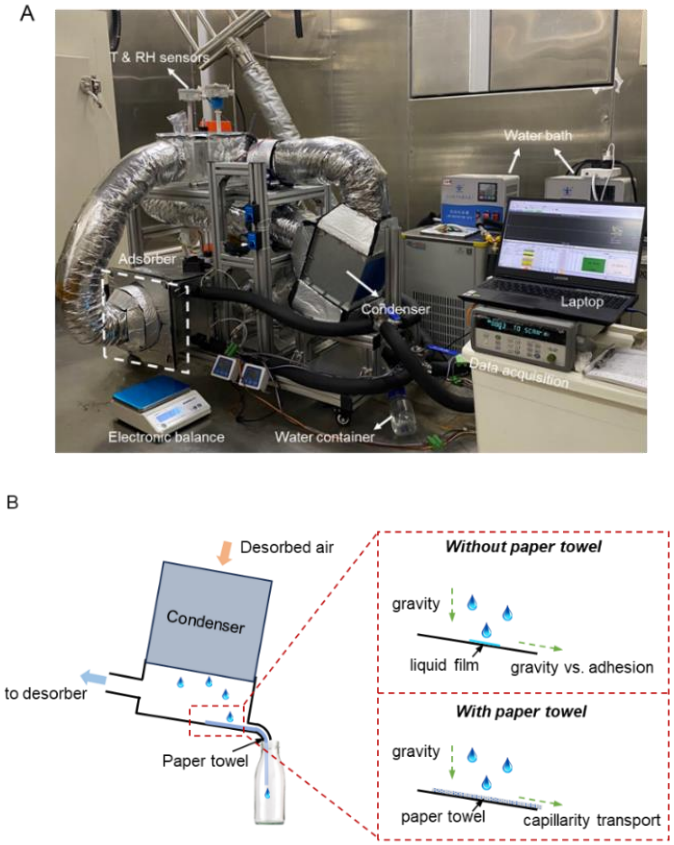

Fig. S17. Water harvesting test in a climate room. To accelerate the water collection rate, we used a paper towel to provide additional capillarity. In this case, once the water droplets fall on the tissue, the water can be transported to the bottle.

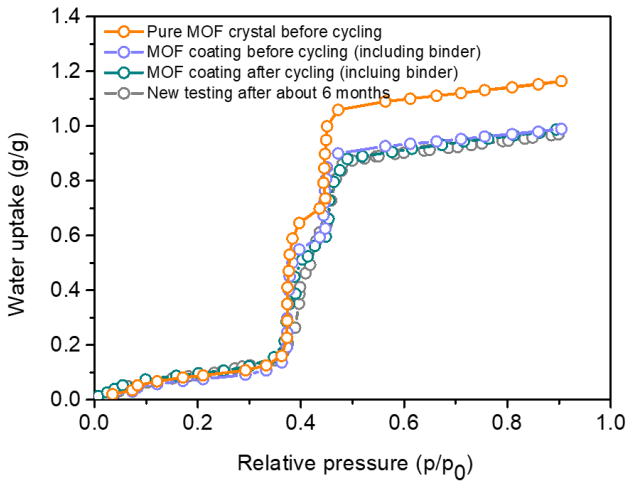

Fig. S18. Water sorption isotherms of pure MIL-101 crystal and composite MOF/binder after cycling at 25°C. New testing is conducted by using MOF in the adsorber after placing at lab for more than 6 months to experience the natural sorption-desorption cycles.

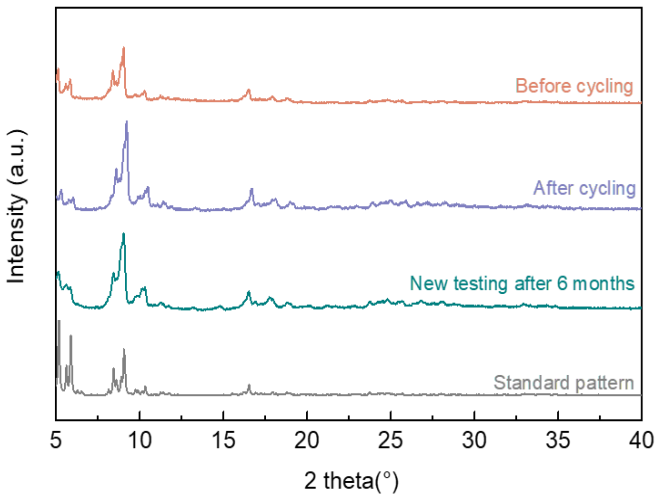

Fig. S19. Powder X-ray diffraction curves of MOF before and after cycling more than 3000 times. New testing is conducted by using MOF in the adsorber after placing at lab for more than 6 months to experience the natural sorption-desorption cycles.

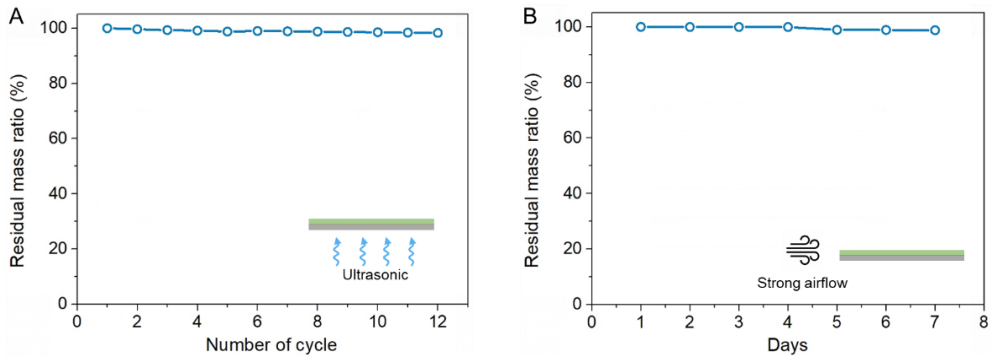

Fig. S20. Stability tests of MOF coating sample. (A) Mass change of MOF coating sample by using ultrasonic meter to simulate the machinal vibration; (B) Mass change of MOF coating sample by strong forced airflow. the MOF coating sample was put in the ultrasonic dispersion meter (FUYANG, F-010SD) to simulate the machinal vibration. After each ultrasonic teat (lasting 20 minutes, 120W), the mass change of coating sample was recorded, indicating that the mass reduction of MOF coating sample was less than 2.7% after 12 times vibration tests. Considering the convective airflow (velocity ~1m/s) is mainly experienced for MOF water harvesters in a real-world application, the stability test is conducted under strong air blowing (>3m/s). As a result, MOF coating still kept 98.79% mass after the test.

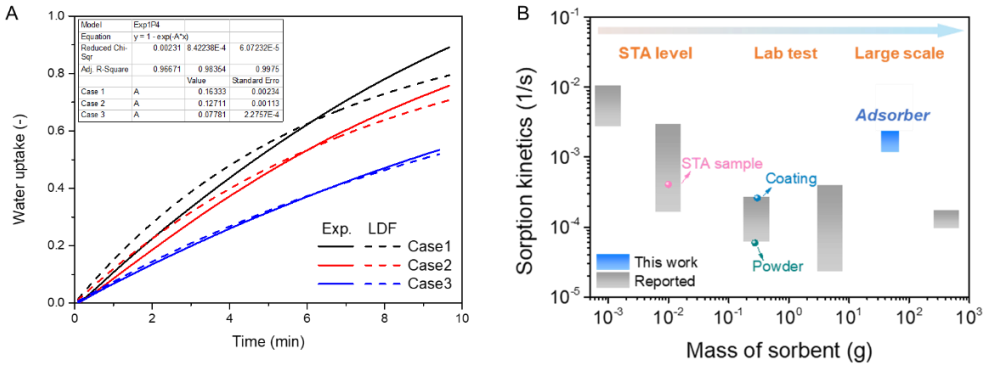

Fig. S21. Dynamic sorption curves of MOF adsorber (A) and comparison of sorption kinetics (B). The results are from the MOF water harvester test under the cooling temperature of 17, 20 and 25°C at 25°C 60%RH, named case 1, 2, and 3, respectively.

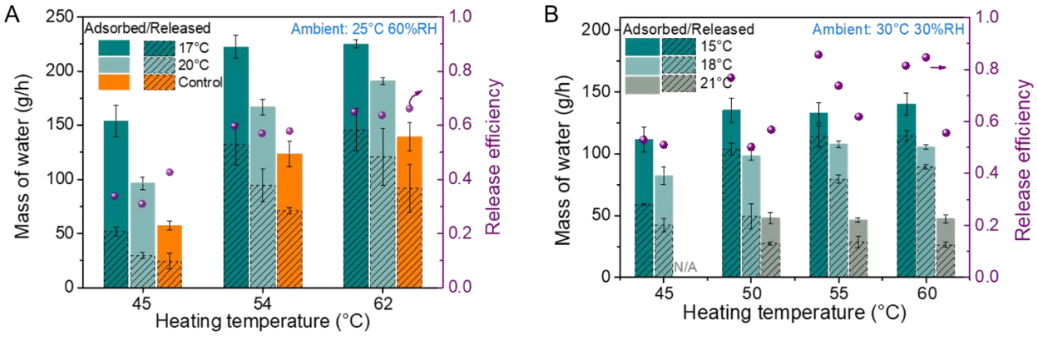

Fig. S22. Mass of adsorbed and released water with different heating temperature at 25°C/60%RH (A) and 30°C/30%RH (B). The low temperature of 45°C is sufficient to drive the MOF water harvester. When the heating temperature is higher than 54°C, the heating energy is sufficient and the improvement of water mass is inconspicuous. Compared with the control case, the release efficiency with the cooling temperature of 20°C is a little lower since more water is captured. But with the decrease of cooling temperature to 17°C, the release efficiency is increased. This further verified that low adsorption temperature contributed to the low condensation temperature to boost the condensation. In this regard, more moisture is liquified and the reduction of humidity in the air circulant provides a bigger humidity difference, promoting the release process.

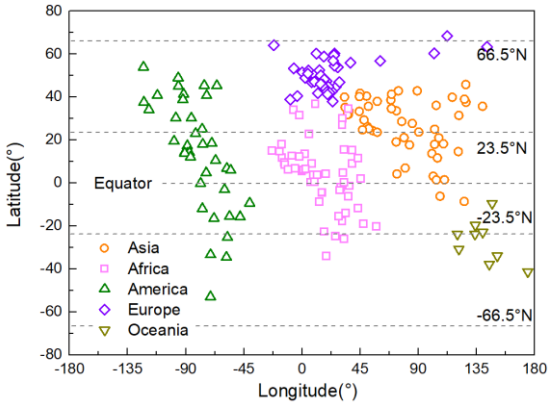

Fig. S23. Locations of selected global cities

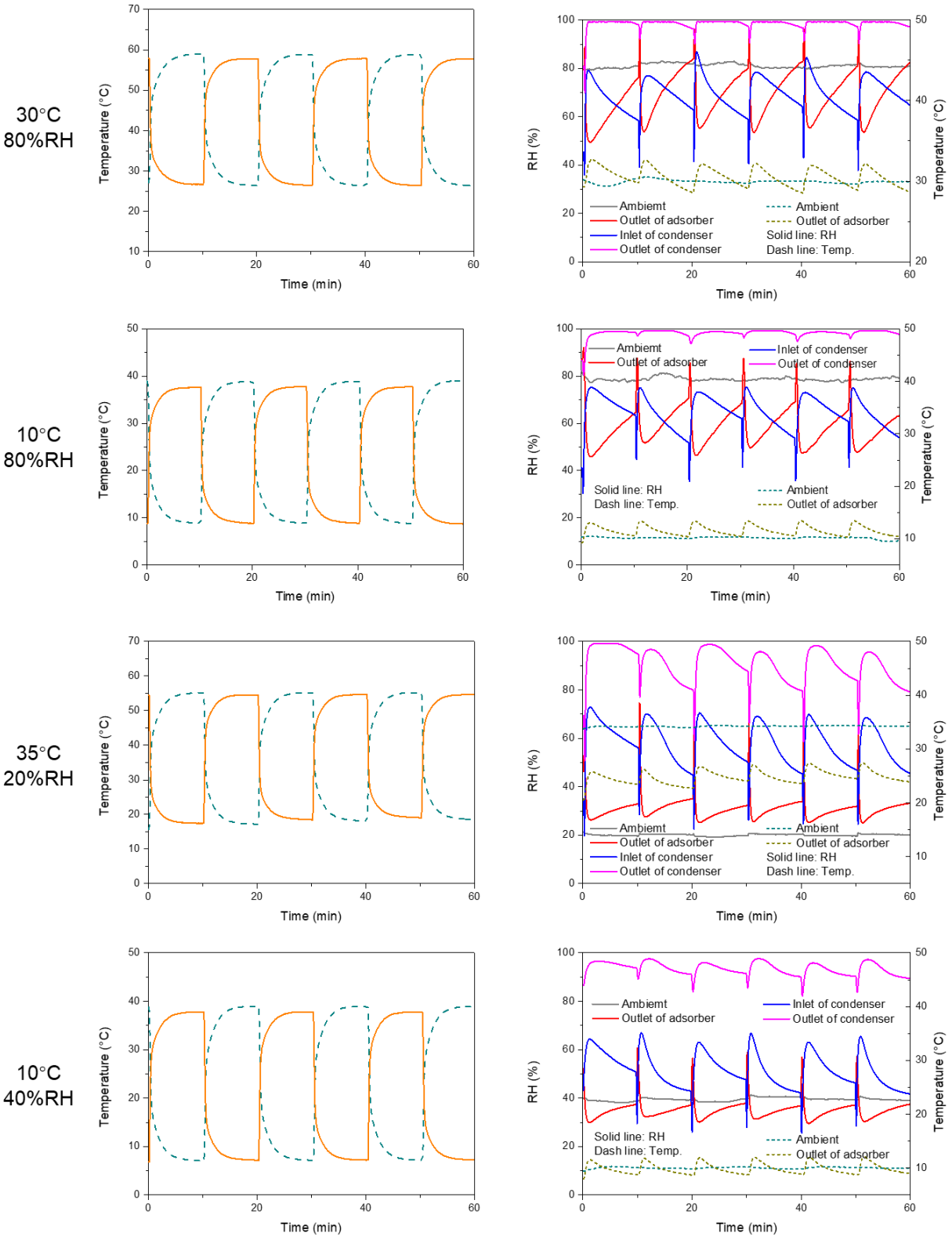

Fig. S24. Test results under the ambient condition of 30°C/80%RH, 10°C/80%RH, 35°C/20%RH and 10°C/40%RH. Cooling and heating temperatures were set as 26/60°C, 8/38°C, 17/55°C and 7/38°C, respectively.

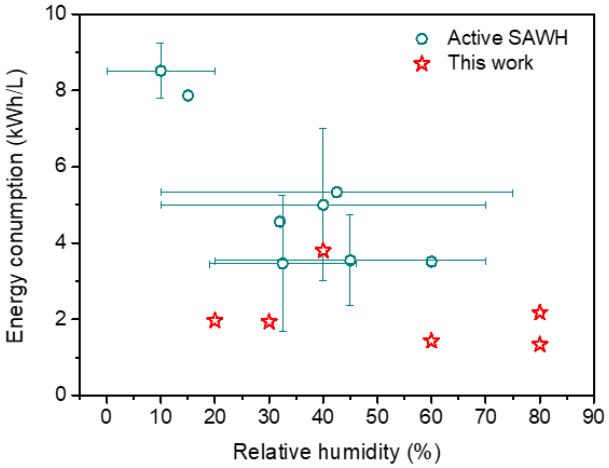

Fig. S25. Energy comparisons between reported active MOF water harvester[2,3] and this work. Due to the variable test condition in the literature, the range of humidity and energy consumption are reflected by the horizontal and vertical lines respectively, and the average value is pointed out. The energy consumption in indoor test was calculated by assuming that the electrical heat pump was used to supply cooling and heating simultaneously. The details could be found in Table S2.

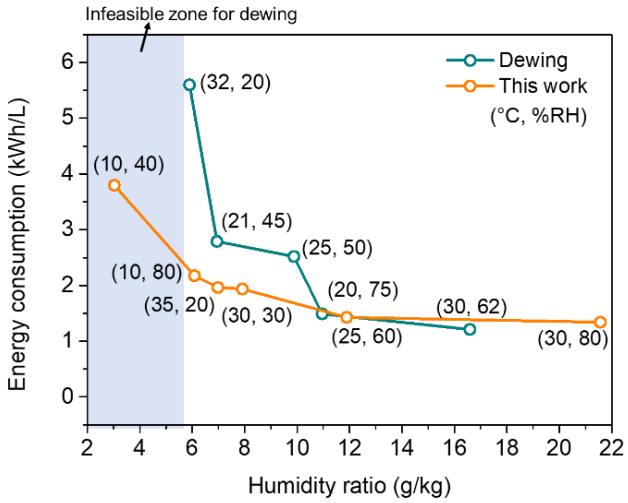

Fig. S26. Comparisons between our work and dewing method[1] at stable weather conditions.

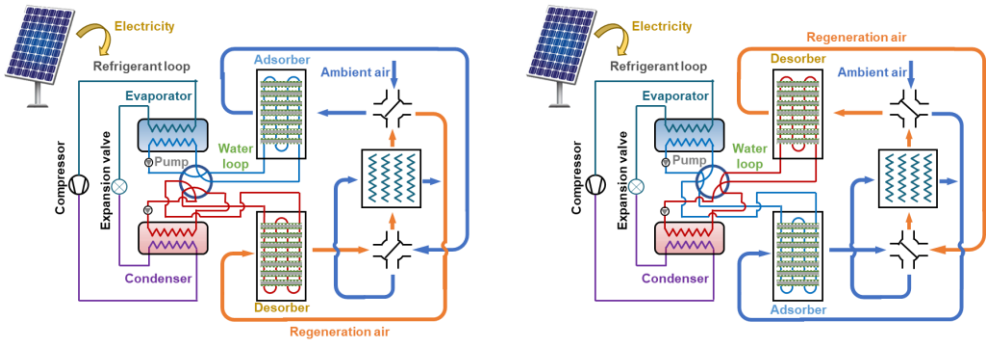

Fig. S27. Scheme of heat pump-integrated MOF water harvester.

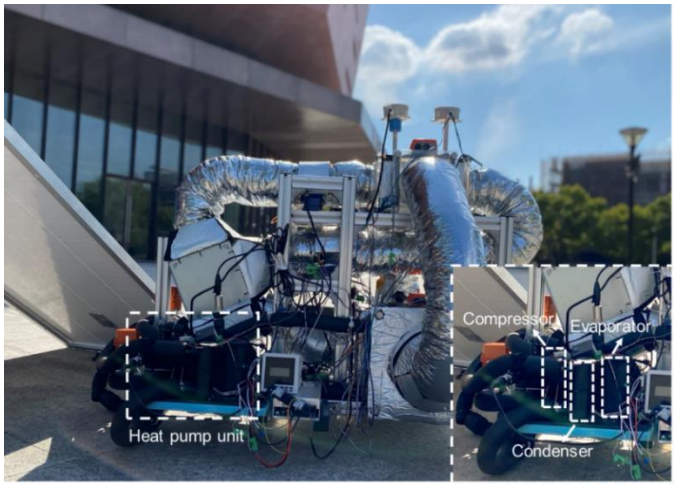

Fig. S28. Backside of MOF water harvester

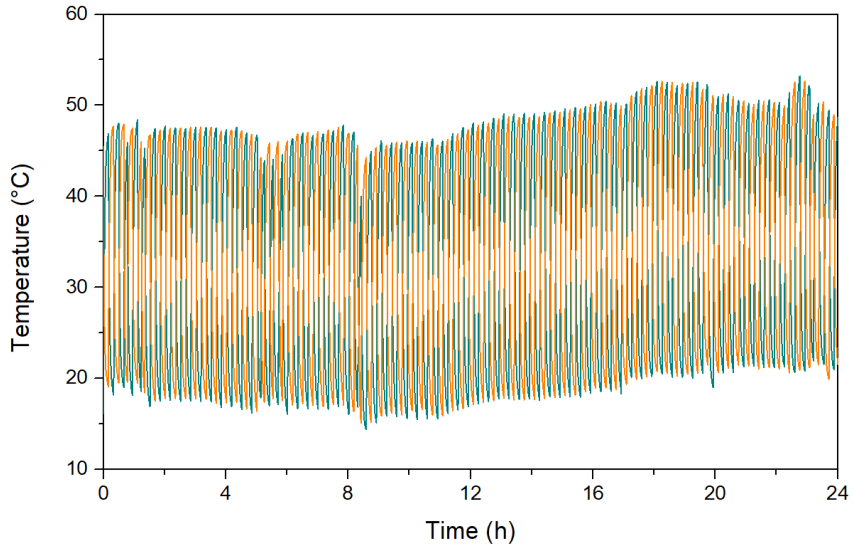

Fig. S29. Cooling/heating temperatures variation with time.

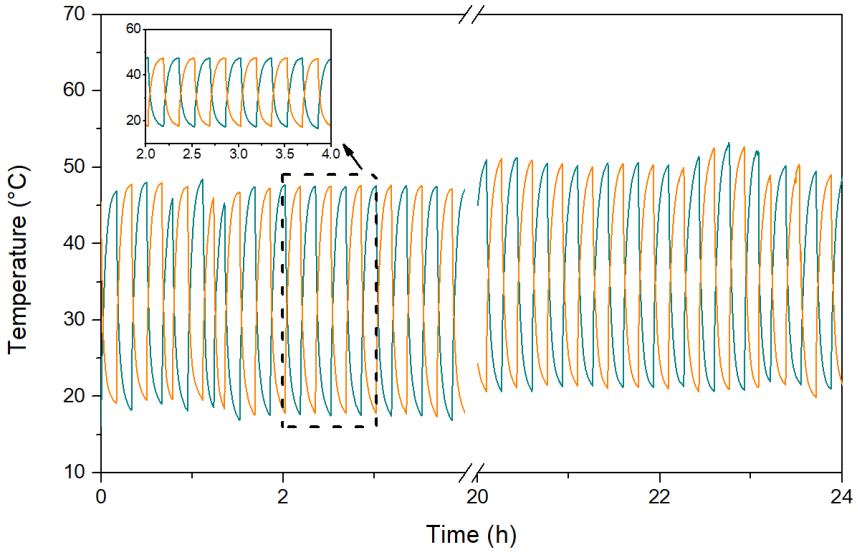

Fig. S30. Detailed cooling/heating temperatures variation with time.

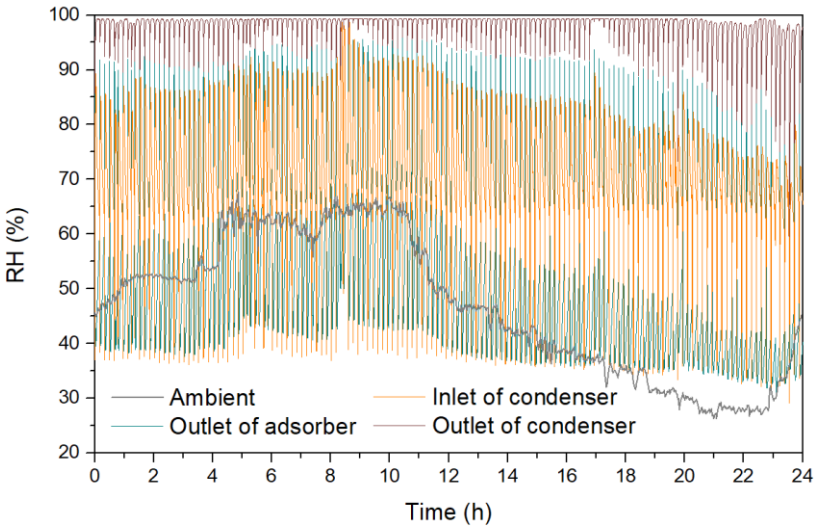

Fig. S31. RH variation with time in practical test.

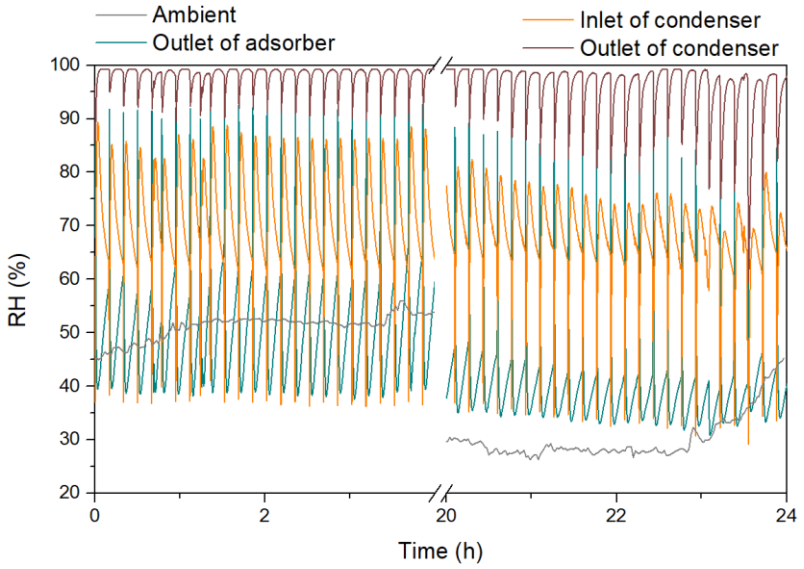

Fig. S32. Detailed RH variation with time in practical test.

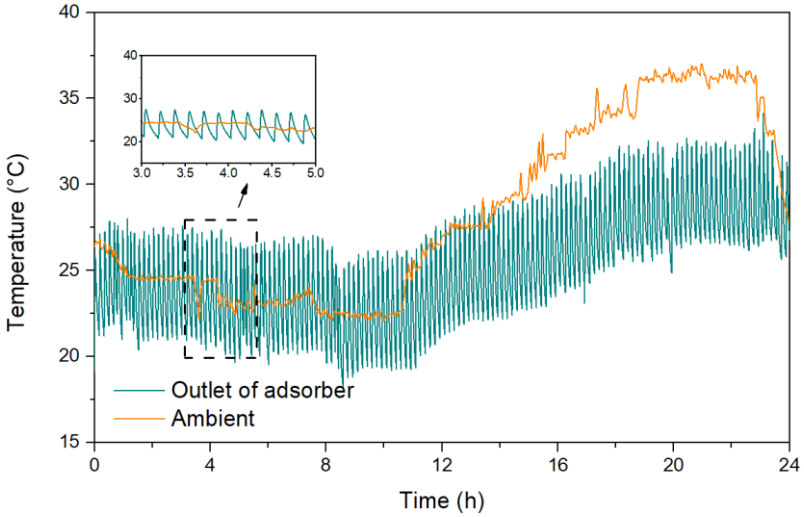

Fig. S33. Temperature variation of ambient and outlet air of adsorber with time.

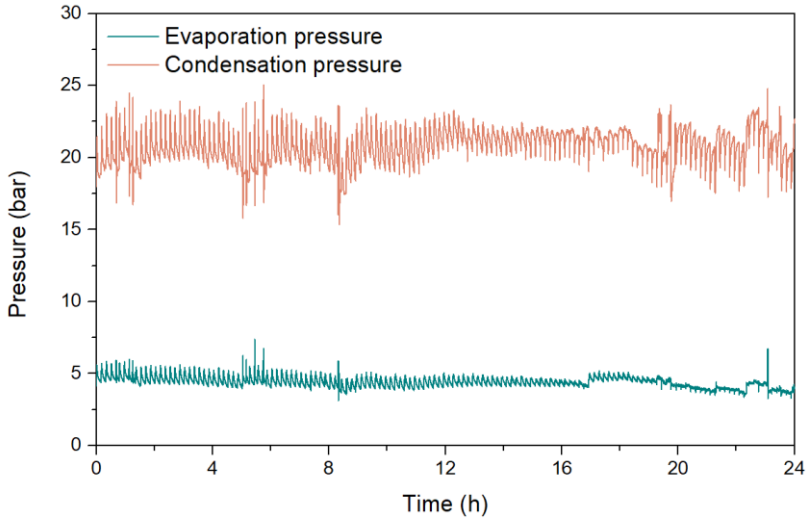

Fig. S34. Evaporation and condensation pressure.

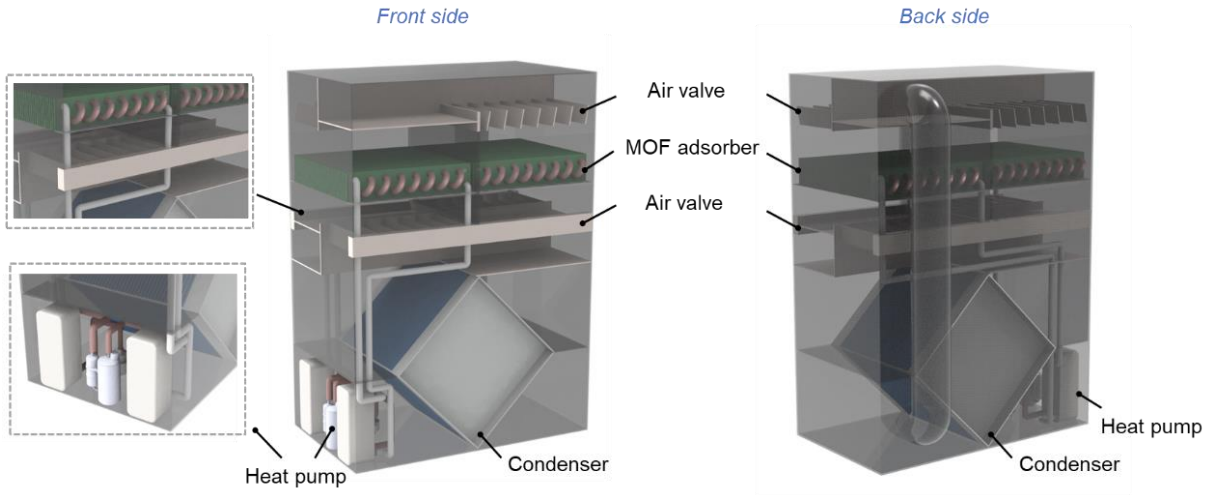

Fig. S35. Possible optimal SAWH design with the same scale of devices used in the experiment. Due to test requirements for experiments, the air duct is relatively complicated in order to get temperature or humidity data. However, for a commercial device, these configurations can be optimized, especially for reducing the volume of auxiliary equipment. This Fig. presents a potential optimization structure of SAWH, all sizes of equipment are the same as the practical scale used in the experiments. As seen, the compact design (426×248×596 mm) can reduce the total volume of SAWH by around 89.4% compared with the experimental design (800×1060×700 mm), and the area (0.106 m^2) could be reduced by 87.5%. In addition, the condenser also can be optimized by using the high-efficiency heat exchanger. In this case, the total volume of SAWH can be further reduced.

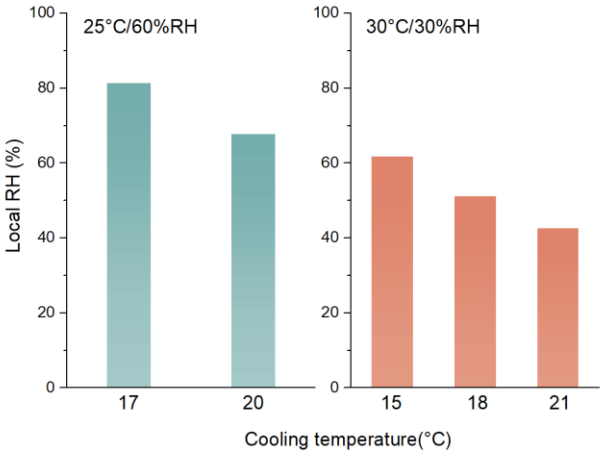

Fig. S36. The local RH with different cooling temperatures considering the temperature margin of 3°C.

The SAWH reported in this work introduced cooling at the sorption stage, the local effective RH near the sorbent would be improved to promote the sorption process. Although the water vapor seems to be close to 100%RH, the heat transfer resistance and condensation efficiency should be taken into consideration.

Considering the temperature margin caused by the heat transfer resistance, the sorbent temperature is assumed to be at least 3°C lower than the cooling temperature from the source[4]. In this case, the local RH with cooling can be found in this Fig., indicating that the cooling at the sorption stage cannot bring the dewing directly.

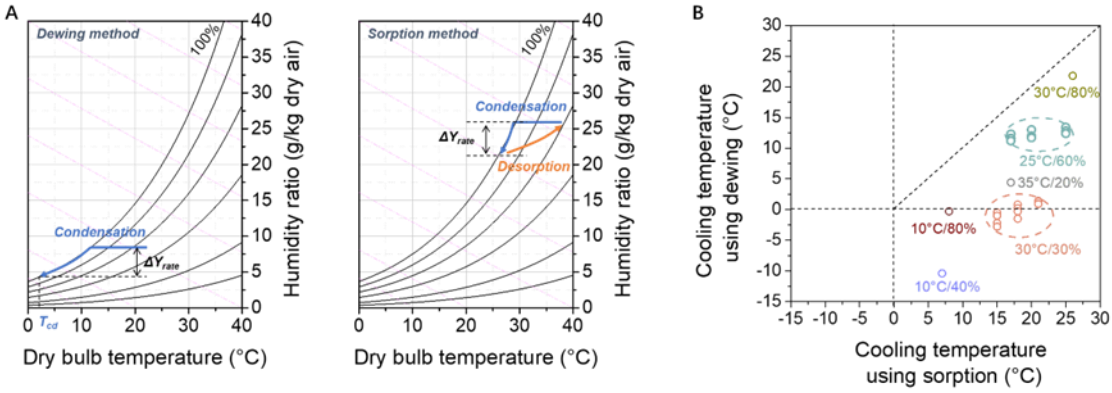

Fig. S37. Comparisons between dewing and sorption method. (A) Air treatment state in the psychrometric chat. (B) Cooling temperature comparisons between sorption and dewing methods with the same productivity.

For the same water harvesting rate, the dewing method should reduce the temperature to T_{cd} (the temperature of cooling source should be at least 3°C lower than T_{cd}). If the same water harvesting rate ($\Delta Y_{rate}=m_w\rho_a^{-1}V_{a,de}^{-1}$) was achieved using dewing method, the cooling temperature using dewing could be determined. It was found that although the cooling was introduced in the sorption method in this work, its cooling temperatures were still higher than that using dewing method, indicating the energy requirement using dewing is harsher than that using sorption. It should be noted that the dewing method cannot access the same productivity with sorption at the relatively arid area since the cooling temperatures are lower than 0°C (10°C/40%, 10°C/80%, 30°C/30%).

Supplementary Tables

Table S1. The mass change before and after shaping MOF

	Before shaping	After shaping	MOF layer (with 15%wt binder)	After adsorption in 25°C 60%RH
HX1	594 g	646 g	52 g	691.5 g
HX2	595 g	643 g	48 g	684.7 g

Table S2. Comparison of loading density

Ref.	Volume of adsorber (L)	Mass of sorbent (g)	Loading density (kg/m^3)	Productivity (L/kg/d)
[3]	52.34	400	7.64	3.5
[5]	42.39	825	19.46	0.067
[6]	2	21.8	10.9	1.05-2.13
This work	1.94*2	100	25.8	7.7-22.8

Table S3. Comparisons between reported active MOF water harvester and this work

MOFs	Weather condition		Productivity (L/kg/d)	Energy (kWh/L)	Continuous or not	Ref.
	Stable	Variable				
MOF-801	40°C/15%RH		1.08	7.87	×	[3]
	25°C/60%RH		2.42	3.51	×	
MOF-303	27°C/32%RH		1.3	4.56	×	[2]
MIL-101	25°C/60%RH		22.81	1.428	√	This work
	30°C/30%RH		18.21	1.936		
	35°C/20%RH		7.75	1.962		
	30°C/80%RH		22.17	1.34		
	10°C/40%RH		11.22	3.797		
	10°C/80%RH		19.06	2.175		
MOF-303		10-27°C/10-75%RH	0.7	5.33	×	[2]
MOF-801		15-35°C/10-70%RH	1.2-2.6	3-7	×	[3]
		RH<20%	0.43-1.58	7.8-9.24	×	
		RH>20%	0.66-2.57	2.36-4.73	×	
		15-35°C/19-46%RH	3.5	1.67-5.25	×	
MIL-101		22-36°C/26-65%RH	9.9	2.96	√	This work

Table S4. Collected water in practical test

Time (h)	Collected water (g)	Cumulative water (g)	Time (h)	Collected water (g)	Cumulative water (g)
1	36.65	36.65	13	42.75	670.52
2	40.31	76.96	14	40.33	710.85
3	40.34	117.3	15	39.18	750.03
4	41.67	158.97	16	41.17	791.2
5	60.38	219.35	17	32.9	824.1
6	58.12	277.47	18	30.32	854.42
7	57.52	334.99	19	28.17	882.59
8	61.26	396.25	20	24.83	907.42
9	62.4	458.65	21	24.41	931.83
10	63.96	522.61	22	21.48	953.31
11	58.76	581.37	23	18.67	971.98
12	46.4	627.77	24	18.43	990.41

Table S5. Costs of sorbent (Unit: USD)

Raw materials	Cost ($/kg)	Consumption (kg/kg$_{MOF}$)	Total cost ($/kg$_{MOF}$)
Terephthalic acid	2.20	1.555	3.421
$CrCl_3 \cdot 6H2O$	0.14	0.969	0.134
DMF	0.814	47.4	38.58
DI Water	0.12	42	5.04
Ethanol	0.8	39.45	31.56
Total cost ($/kg$_{MOF}$)			78.735

Table S6. Costs of device (Unit: USD)

Component	Cost ($)	Component	Cost ($)
Heat exchanger	4.14	Copper tube	0.3
Condenser	13.79	Acrylic	16.55
Refrigerant	0.38	Valve	22.07
Compressor	55.18	Actuator	11.04
Plate heat exchanger	22	Air duct	2.76
Air Fans	55.16	Insulation	1.17
Pump	7.45	Pipe	3.31
Total cost ($)	215.3		

Table S7. Comprehensive comparisons between reported works and this work

Mode	Weather condition	Material	Adsorber unit		Device		Cycles /day	Energy (kWh/L)	Ref.
		$L_{H2O}/kg_{sorbent}$/ day	$L_{H2O}/L_{adsorber}$/day	L_{H2O}/m_{wind}^2/ day	g_{H2O}/L_{device}/ day	g_{H2O}/kg_{device}/day			
Active	10-35°C/ 20-80%RH	7.78-22.8	0.2-0.59	18.09-53.02	1.31-3.84 12.37-36.25(opt.)	37.53-110	144	1.34-3.80	This work
	22-36°C/ 26-65%RH	9.9	0.26	23.02	1.67 15.72 (opt.)	47.76	144	2.96	This work
	27°C/32%RH	1.3	0.09	20.10	6.29		9	4.56	2
	10-27°C/ 10-75%RH	0.7	0.065	14.48	4.53		9	5.33	2
	15-35°C/ 10-70%RH	1.2-2.4	0.009-0.018	4.40-8.81	1.64-3.27		18	3-7	3
	19-46%RH	1.8-3.5	0.014-0.027	6.61-12.84	2.45-4.77		6-30	1.67-5.25	3
Passive	10-15°C/ 40%RH	0.067	0.0013	0.26	0.69		1	-	5
	30°C/30%RH	2.13	0.023	4.64	17.52	32.91	8	-	6
	30°C/42-70%RH	1.05	0.011	2.82	8.63	16.18	8	--	6
	20°C68%RH	0.11	0.048	0.153	5.17		1	-	7
	10-20°C/ 40-65%RH	1.09	0.312	0.623	55.66	97.40	8	2.22	8

Table S8. Material-, device-, and system-based parameters for MOF water harvester

Sorbent	Produced water (g)	Material	Adsorber unit		Device		Ref.
		Mass of sorbent (g)	Volume (L)	Area (m^2)	Volume (L)	Weight (kg)	
MIL-101	778-2281	100	1.94*2	0.043	593.6 62.97 (opt.)	20.73	This work
MOF-303	562.9	433	7.01	0.028	89.43	-	2
	405.3	579	7.01	0.028	89.43	-	2
MOF-801	480-1400	400	52.34	0.109	293.38	-	3
MOF-801	55	825	42.39	0.209	79.37	-	5
LiCl@rGO-SA	22.82-46.42	21.8	2	0.01	2.65	1.41	6
AQSOA Z01	59.7	520	0.624*2	0.195*2	11.55	-	7
ACF-LiCl	311.69	286	1	0.0625*8	5.6	3.2	8

Table S9. Concentrations of metals in collected water

Metals	Concentrations (mg/L)	WHO Guideline (mg/L)	National standard of China (mg/L, GB5749-2022)
Zn	0.648	3.0	1.0
Al	0.053	0.2	0.2
Cu	N/A	2	1.0
Fe	N/A	0.3	0.3
Pb	N/A	0.01	0.01
Cr	N/A	0.05	0.05
Ba	N/A	1.3	0.7
Ni	N/A	0.07	0.02
Mn	N/A	0.1	0.1
Cd	N/A	0.003	0.005
Hg	N/A	0.006	0.001
Se	N/A	0.04	0.01

Table S10. Concentrations of Ions in collected water.

Ions	Concentrations (mg/L)	WHO Guideline (mg/L)	National standard of China (mg/L, GB5749-2022)
F^-	N/A	1.5	1.0
Cl^-	0.386	250	250
Br^-	N/A	0.5	0.01
NO_3^-	0.960	50	10
NO_2^-	0.198	3	N/A
SO_4^{2-}	6.090	250	250
Li^+	0.0014	N/A	N/A
Na^+	3.713	200	200
NH_4^+	5.1953	N/A	N/A
K^+	0.709	200	N/A
Ca^{2+}	0.010	200	N/A
Mg^{2+}	0.0678	200	N/A

Supplementary Notes

Note S1. Thermodynamic analysis

The principles of directing dewing, traditional method and our design are described in Fig. S1-1. For a cooling-based AWH, the air needs to be cooled below the dew point. Thus, the outlet air condition is determined as T_{cond} and 100%RH.

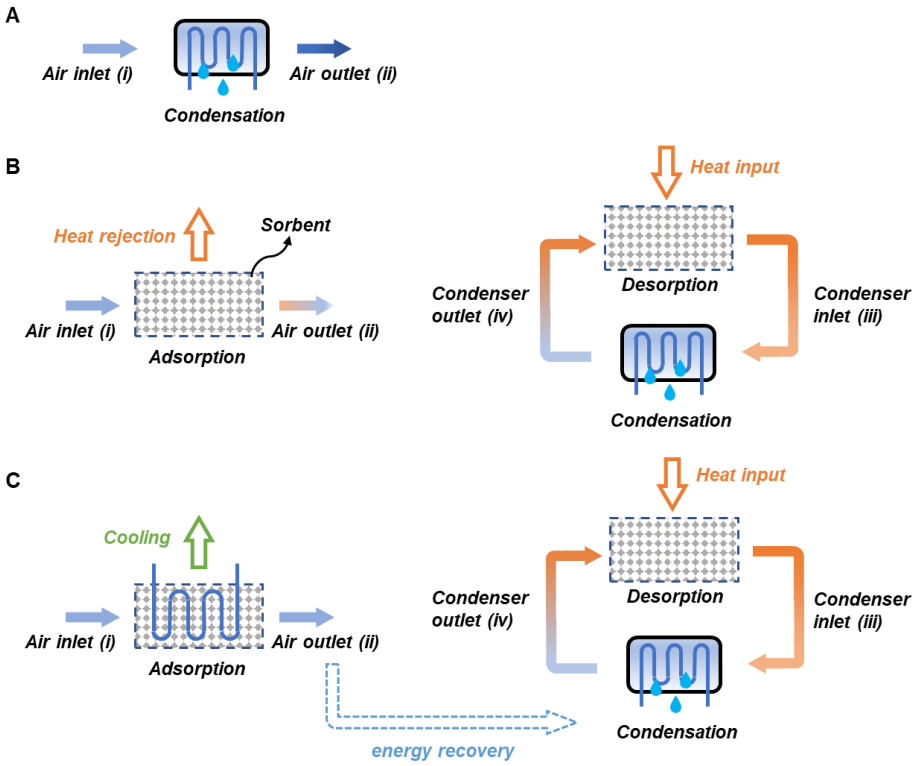

Fig. S1-1. Principe of water harvesting technologies. (A) Direct dewing method. (B) Traditional SAWH. (C) SAWH with cooling at sorption stage.

Then the cooling capacity can be calculated by the enthalpy difference between inlet air and outlet air, as expressed by

$$Q_{c,\,dewing}=m_a\left(h_{a,in}-h_{a,o}\right) \tag{S1}$$

where m_a means the mass of air, and the $h_{a,in}$ and $h_{a,o}$ refer to the enthalpy of inlet air and outlet air, respectively. Mass of air and water should be satisfied with mass conservation as

$$m_a\left(Y_{a,in}-Y_{a,o}\right)=m_w \tag{S2}$$

where m_e is the mass of water, and $Y_{a,in}$ and $Y_{a,o}$ present the humidity ratio of inlet air and outlet air, respectively. In this case, we assumed that the realistic recovery ratio of air treatment is 0.5, which is determined by the ratio of humidity ratio difference between inlet and outlet air to that of ambient air ($RR=(Y_{a,in}-Y_{a,o})/ Y_{a,in}$). According to the mass conservation in Equation (S2), the Equation (S1) can be expressed by

$$Q_{c,AWH}=\frac{m_w\left(h_{a,in}-h_{a,o}\right)}{Y_{a,in}-Y_{a,o}} \tag{S3}$$

For the traditional sorption-based AWH, the required heating energy input at the desorption stage can be expressed by

$$Q_{in,H}=\left[\frac{m_w c_{p,s}}{W_d}+m_w c_{p,w}+m_{a,de}\left(c_{p,a}+Y_{s,in}c_{p,v}\right)\right](T_H-T_{cond})+m_w h_{ad} \quad \text{(S4)}$$

where $c_{p,s}$, $c_{p,w}$, $c_{p,a}$ and $c_{p,v}$ are specific heat capacity of sorbent, water, air and vapor, respectively. W_d is water uptake, and T_H and T_{cond} represent the temperature of heating and condensation, and h_{ad} means the desorption enthalpy. The first term of RHS (right hand side) refers to sensible heat consisting of heating energy for sorbent, water and air. The second term of RHS is latent heat for desorption.

The humidity ratio of the sorbent unit inlet is determined by the condensation temperature, as expressed,

$$Y_{s,de,in}=Y_{cond,out}=Y(T_{cond},\ 100\%RH) \quad \text{(S5)}$$

The humidity ratio of the sorbent unit outlet can be derived as

$$Y_{s,de,out}=\frac{\int_{T_{H,min}}^{T_H} Y(RH_{de},T)\,dT}{\Delta T} \quad \text{(S6)}$$

The minimum desorption temperature $T_{H,min}$ can be calculated based on the outlet air state of condenser and the isotherms, as expressed by

$$T_{H,min}=T\left(T_{cond},\ RH_{de,min}\right) \quad \text{(S7)}$$

Herein, the $RH_{de,min}$ can be determined from sorbent isotherms, which refers to the lowest RH of operational humidity windows for MOFs, as shown in Fig. S1-2. The isotherms of MOF-801[9], MOF-303[2], Al-fumarate[2], and BTDD[10] are from the literature.

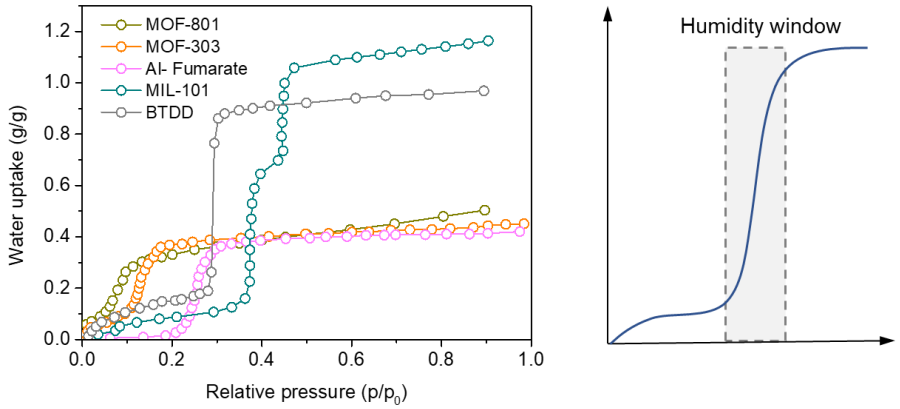

Fig. S1-2. Isotherms of common water sorbing MOF.

Similarly, for AWH with cooling-enhanced sorption, besides heating energy for desorption which can be calculated by Equation (S4), the cooling capacity of adsorption can be expressed as

$$Q_{in,C}=\left[\frac{m_w c_{p,s}}{W_d}+m_w c_{p,w}+m_{a,ad}\left(c_{p,a}+Y_{s,in}c_{p,v}\right)\right](T_{am}-T_{ad})+m_w h_{ad} \quad \text{(S8)}$$

where T_{ad} is the adsorption temperature (sub-ambient temperature), which is assumed as the same as the optimal temperature of the cooling source. The first and second terms of RHS represent the sensible (including heating energy for sorbent, water and air) and latent heat, respectively. We also assumed that

the recovery ratio at sorption stage is 0.5 to conduct a comparison since the outlet air state could be determined by different airflow rate.

The selection of cooling source should be optimized at the minimum energy consumption as Equation (S9). Lower temperature will lead to a higher water uptake but increased energy consumption. Especially when effective RH near the sorbent is higher than step RH, water uptake will not be improved further.

$$T_{ad}=T\left\{min\ Q_{in,C}\right\} \tag{S9}$$

And the water uptake is determined by the effective RH and temperature by isotherm, as shown in Equation (S10).

$$\begin{cases} W_d=f_{iso}(T_{ad},RH_{ad}) \\ RH_{ad}=\dfrac{p_{vs}(T_{am})RH_{am}}{p_{vs}(T_{ad})} \end{cases} \tag{S10}$$

To conduct a fair comparison, the cooling energy consumption should be transferred into the heating energy form. Previous work transferred it into thermal energy consumption by the ideal heat engine and refrigerator[11]. However, the grade of heat engine is often over the 400°C. Given that the temperature grade of ca. 100°C (or lower than 100°C) in traditional sorption based AWH, we assumed that the cooling capacity can be provided by a vapor compression cycle with COP of 5[12,13], which can be driven by the photovoltaic panels with efficiency of 20%[7,14]. Total energy consumption can be expressed as

$$Q_{in}=\frac{Q_{in,C}}{COP\cdot\eta_{PV}}+Q_{in,H} \tag{S11}$$

The isotherms are fitted by the functions between water uptake and sorption potential (ΔF). Sorption potential (or free sorption energy) is determined by the relative pressure and related temperature,

$$\Delta F=-RTln\frac{p_v}{p_{vs}} \tag{S12}$$

where R is the gas constant (J mol^{-1} K^{-1}), p_v and p_{vs} are the water vapor pressure and the saturated vapor pressure at the given temperature, respectively. Therefore, the temperature and RH can be unified into one factor ΔF. The fitting results are shown in Fig. S1-3.

To evaluate the thermodynamic performance with different method or sorbents, the thermal efficiency η_I is derived as

$$\eta_I=\frac{m_w h_{fg}}{Q_{in}} \tag{S13}$$

where the h_{fg} means the latent heat of water condensation. The maximum thermal efficiency is determined by the minimum energy consumption. The minimum energy consumption for water harvesting can be calculated by the specific exergy difference based on the Carnot cycle existing at heat source (T_H) and heat sink (T_0), which can be derived as

$$Q_{H,min}=\frac{m_a\Delta e_a+m_w e_w}{1-\dfrac{T_0}{T_H}} \tag{S14}$$

where the m and e mean the mass and specific exergy, and subscripts a and w present the air and water, respectively.

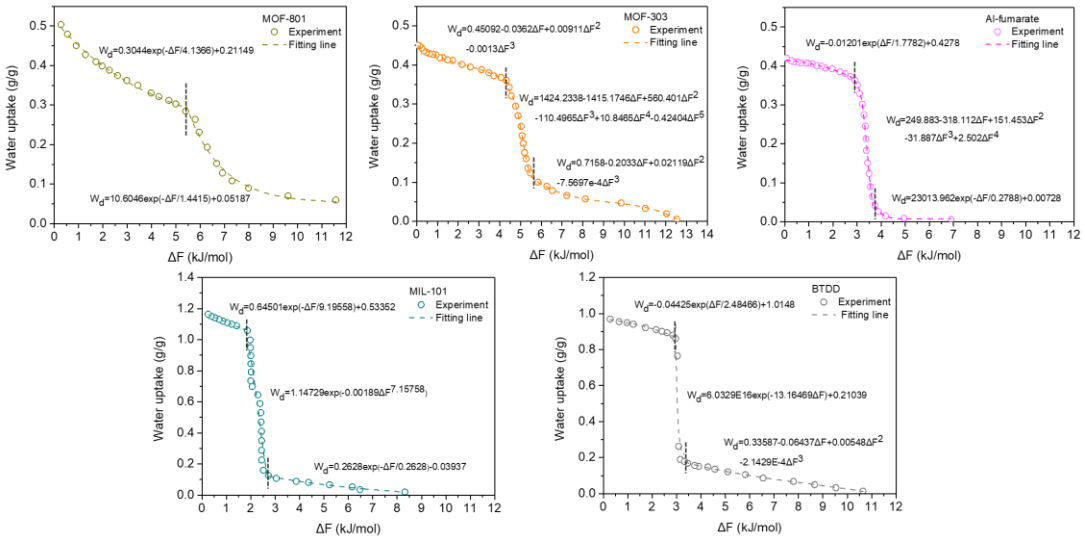

Fig. S1-3. Fitting isotherms with sorption potential theory

Therefore, the second law efficiency which refers to the thermodynamic perfection can be calculated by

$$\eta_{II}=\frac{Q_{H,min}}{Q_{in}} \tag{S15}$$

The air treatment process of dewing method, sorption-based AWH and SAWH with cooling-enhance sorption can be found in Fig. S1-4. As indicated, the air temperature should be lower than the dew point to produce liquid water, while the sorption method could elevate the dew point by sorption-desorption cycle and the water can be liquified at the ambient temperature (Fig. S1-4 A-B).

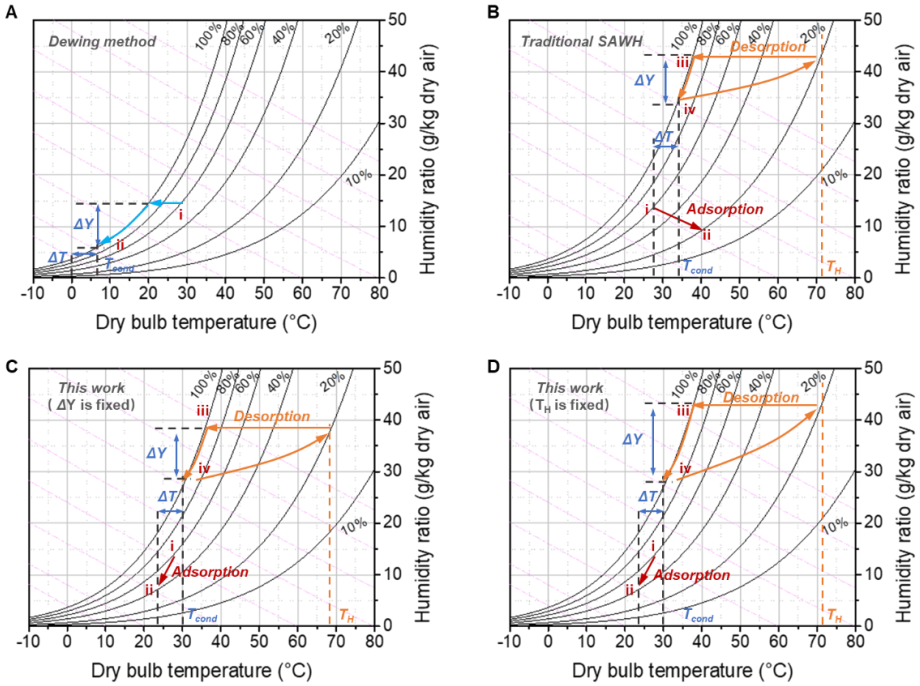

Fig. S1-4. Air treatment processes using different water harvesting technologies. (A) Dewing method. (B) Traditional sorption-based AWH. (C) and (D) Water harvesting with cooling-enhanced sorption with

constant water harvesting rate (C) and constant heating temperature (D).

Accordingly, the sorption is a typical exothermic process, therefore the outlet air temperature of sorption will be increased, which is not conductive to sorption. For the sorption with cooling, the sorption heat will be overcome by the cooling source, then the waste energy from the sorption could be a cooling source for the condensation process, which further reduced the desorption temperature if the water harvesting rate (ΔY) is fixed (Fig. R15C). When using the same heating temperature, the ΔY will be increased (Fig. R15D). Although the cooling energy is required for this method, the requirement of cooling is far away higher than that of dewing method.

Based on the above principle, we assumed that the condensation temperature is 5°C higher than the lowest temperature (ambient temperature for dewing and traditional SAWH while cooling temperature for this work) considering the heat transfer margin. The typical thermal efficiency is drawn in the Fig. S1-5 for the validation of the thermodynamic analysis with the experimental results from literature[2,9]. As seen, the higher thermal efficiency could be reached with higher heating temperature, while the deviations between experiments and models are caused by the actual heat loss. The higher desorption temperature, the higher heat loss.

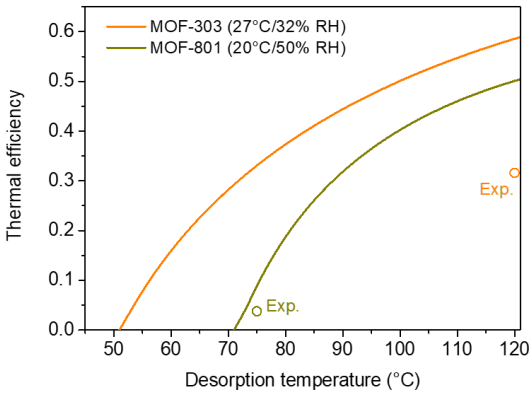

Fig. S1-5. Thermal efficiency with MOF-303 and MOF-801 using reported results.

Firstly, we evaluate the thermal efficiency and second law efficiency using traditional SAWH and direct dewing method (refrigeration), as indicated in Fig. S1-6. Since the dewing method is not based on the cooling energy consumption if the recovery ratio is fixed, its thermal efficiency is constant as a base line. Due to the increased minimum energy requirement for high temperature, the second law efficiency is reduced with increased heating temperature. As shown in Fig. S1-6, the minimum desorption temperature is tightly related with the sorption step point. MIL-101 with step at high pressure has the advantage of low-temperature driven desorption, which is consistent with our primarily thermodynamic analysis. The microporous MOFs (e.g., MOF-801 and MOF-303) with step at low pressure could capture more moisture at arid climate, but the required desorption temperature is high. Besides the mild or humid climate (25°C/60%RH and 30°C/80%RH), when the weather is changed to the low humidity or low temperature condition (10°C/80%RH, 10°C/40%RH, and 35°C/20%RH), the refrigeration technology with direct dewing cannot work due to the potential problem for frosting when dew point is lower than 0°C.

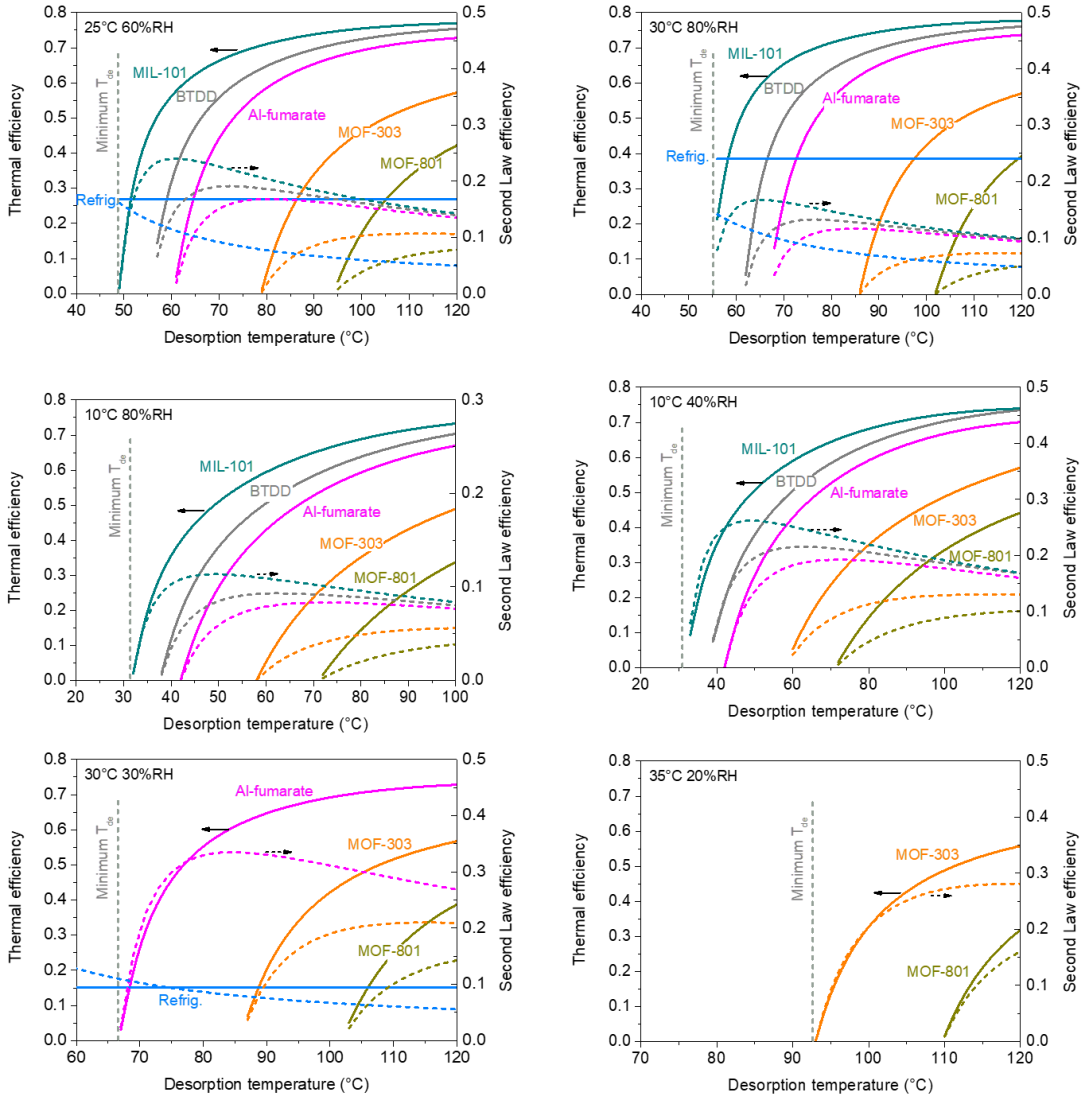

Fig. S1-6. Thermal efficiency and second law efficiency using different sorbent and refrigeration technology at different weather condition. The recovery ratio of sorption process is assumed as 0.5. The cooling COP for refrigeration is assumed as 3.

Although MIL-101 has the high efficiency, it cannot be used for arid climate (30°C/30%RH and 35°C/20%RH). In this case, the microporous MOFs has the great potential for using in ultra-low humidity area. As mentioned above, the weather variation also should be taken into consideration. Once the microporous MOF is used to adapt the arid climate, the energy efficiency became lower than mesoporous MOF when encountering humid environment. To this end, the adaptivity and energy cost should be a tradeoff problem. Furthermore, one question is raised- how can we use the MOF when ambient RH is beyond its useful zone? That motivated us to introduce cooling actively into sorption stage.

As presented in Fig. S1-7, once the cooling sorption is employed, the suitable working zone of MOF can be externed. For 30°C/30%RH, the MIL-101 and BTDD will work and Al-fumarate is still effective in 35°C/20%RH. The thermodynamic analysis indicates the although the total energy consumption is increased with cooling for mesoporous MOFs (leading to lower thermal efficiency compared with that under humid environments), there still exists advantages for them at the low-temperature driven desorption process compared with microporous MOFs. At 30°C/30%RH, the MIL-101 can be driven by

the low temperature of 50-70°C with a competitive thermal efficiency. And for 35°C/20%RH, the MIL-101, BTDD and Al-fumarate with cooling could also be used with high efficiency and low desorption temperature below 90°C. From a view of second law efficiency, low-grade thermal energy has a high quality of energy, resulting a high second law efficiency. Therefore, using low-grade thermal energy is conductive to energy-efficient AWH, which also could be driven by the enormous waste heat.

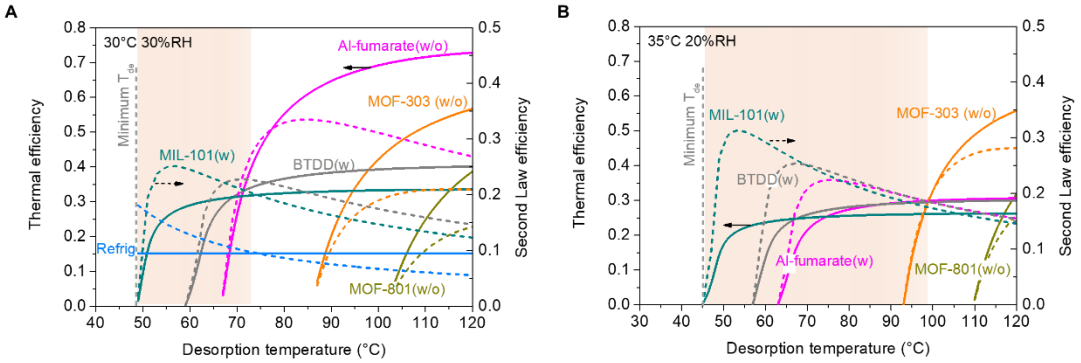

Fig. S1-7. Thermal efficiency and second law efficiency using different sorbents with ("w") and without ("w/o") cooling at sorption stage.

Actually, for the sorption-based AWH, different desorption temperatures lead to different water productivities. In this case, we would like to compare the specific energy consumption with the same water yield. Considering the different energy forms of thermal and electrical energy, specific exergy consumptions (kJ exergy per kg water) are carried out by Equation (S16),

$$E_x = Q_H\left(1-\frac{T_0}{T_H}\right)+Q_C\left(\frac{T_0}{T_C}-1\right) \tag{S16}$$

For dewing method, only the cooling exergy is included at given ΔY, and thus the condensation temperature can be decided. The boundary of dewing method is determined by the condensation temperature of 0°C. For the traditional sorption AWH, only the heating exergy in included while the heating temperature is decided by the given water production rate (ΔY). For the SAWH with cooling-enhanced sorption, both the heating and cooling exergies are calculated. The sorption temperature is derived by the optimal cooling temperature at the minimum exergy consumption. The optimal working zone of different technologies can be determined at the minimum exergy consumption at given water production rate, which can be identified in Fig. S1-8. With cooling-enhanced sorption, we could extend the suitable zone for sorption-based AWH with efficient sorbent.

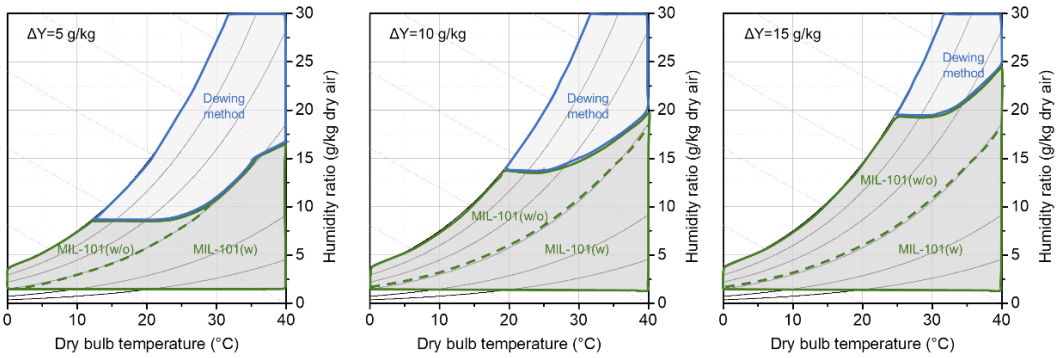

Fig. S1-8. The exergy-optimal zone at different water harvesting rate for dewing method and sorption method with MIL-101.

Note S2. Mechanism of cooling-enhanced sorption.

Simulation of temperature, humidity and concentration fields

The physical model is based on our dynamics test in Figure 1G. The MOF sorbent was coated on the aluminum sheet with a size of 60×1mm (W×H), and the thickness of MOF coating layer is 0.3mm. The experiments and simulation were conducted at a natural airflow without forced convection. The governing equations are developed based on the following assumptions: (1) the pore structure, porosity and tortuosity are homogeneous and constant; (2) The thermal properties are constant; (3) Desorption enthalpy is assumed as a constant (2600 J/g).

The heat transfer equations in air side and sorbent side are respectively derived from:

$$\rho_a C_{pa} \frac{\partial T}{\partial t} + \rho_a C_{pa} \vec{u} \cdot \nabla T = \nabla \cdot \lambda_a \nabla T \tag{S17}$$

$$\rho_s C_{ps} \frac{\partial T}{\partial t} = \nabla \cdot \lambda_s \nabla T + Q \tag{S18}$$

The sorption heat Q is calculated as

$$Q = h_{ads} \frac{\partial x}{\partial t} \tag{S19}$$

where the dynamics sorption ∂w/∂t can be calculated by the linear driving force (LDF) model (see Note S2). The mass transfer equation in air side and sorbent side are respectively calculated as

$$\frac{\partial c_a}{\partial t} - D_a \nabla c_a + \vec{u} \cdot \nabla c_a = 0 \tag{S20}$$

$$\frac{\partial c_s}{\partial t} - D_{eff} \nabla c_a + \frac{1-\varepsilon_s}{\varepsilon_s} \rho_s \frac{\partial x}{\partial t} = 0 \tag{S21}$$

The effective diffusivity D_{eff} is approximated as surface diffusivity D_S, and the water vapor diffusivity D_a inside pore is calculated by the molecular diffusivity and Knudsen diffusivity[15],

$$D_{eff} \approx D_s = \frac{\varepsilon}{\tau} 1.6 \times 10^{-6} \exp\left(-0.974 \times 10^{-6} \frac{h_{ads}}{T}\right) \tag{S22}$$

$$D_a = \frac{\varepsilon}{\tau} \left(\frac{1}{D_M} + \frac{1}{D_K}\right)^{-1} \tag{S23}$$

$$D_M = D_0 \frac{p_0}{p} \left(\frac{T}{T_0}\right)^{1.5} \tag{S24}$$

$$D_K = \frac{d_s}{3} \sqrt{\frac{8RT}{\pi M}} \tag{S25}$$

The bottom surface temperature of aluminum is set at constant cooling temperature as a boundary condition, and the other walls was treated as an open side where the temperature and humidity are the same as the ambient conditions. All parameters used in the model as listed and explained in the Table S2-1.

Table S2-1. Parameters used in the model

Symbol	Explanation	Value
ρ_a (kg/m3)	air density	From the database in COMSOL
Cp_a (J/g/K)	specific heat capacity of air	
λ_a (W/m/K)	heat conductivity of air	
ρ_s (kg/m3)	sorbent density	391
Cp_s (J/g/K)	specific heat capacity of sorbent	1.0
λ_s (W/m/K)	heat conductivity of sorbent	0.2

h_{ads} (J/g)	desorption enthalpy	2600
ε_s	porosity	0.8
τ_s	tortuosity	2
R (J/mol/K)	gas constant	8.314
M (g/mol)	water molecular mass	18
d_s (μm)	characteristic diameter of sorbent	0.75

The simulation was conducted by COMSOL Multiphysics. From the macroscope view of temperature and humidity fields, we can find that the reforming gradient at the interface between air and sorbent (ambient condition of 25°C/60%RH and 30°C/30%RH), as shown in Fig. S6. Once the cooling is introduced into sorbent, the temperature and humidity gradient at the interface between air and sorbent will be changed, resulting in an increased humidity, which could promote the sorption process. The water vapor concentration difference between bulk air and sorbent trigged the water molecular movement.

Chemical potential.

From the basic chemical potential insight, here we also try to explain the mechanism of triple benefits from thermodynamics view. The movement of water molecules can be theoretically described by their chemical potential (μ_{H2O}), which is defined as the partial molar Gibbs free energy[16]:

$$\mu_{H2O}=\mu^{\theta}_{H2O}+RTln\left(p_v/p^{\theta}\right) \quad \text{(S26)}$$

where the μ^{θ}_{H2O} is the chemical potential of water in its standard state (-228.6 kJ/mol for gaseous state and -237.15 kJ/mol for liquid state), R, T and p_v and p^{θ} present the gas constant (8.314 J/mol/K), temperature, water vapor pressure and atmosphere pressure (101325 Pa).

The water vapor pressure can be expressed by the relationship with saturated water vapor pressure (p_{vs}) and relative humidity (RH)

$$p_{H2O}=p_{vs}\,RH \quad \text{(S27)}$$

When the chemical potential of atmospheric water ($\mu_{H2O,a}$) is higher than that of sorbed water ($\mu_{H2O,s}$), sorption occurs. In this condition, the difference in chemical potential between air and sorbent is the driving force for AWH. For the desorption process, the heating process increases the chemical potential of atmospheric water, and once it is higher than the chemical potential in the condensation surface ($\mu_{H2O,cd}$), the water condensation is trigged. The pathways of AWH can be described in Fig. S2-1.

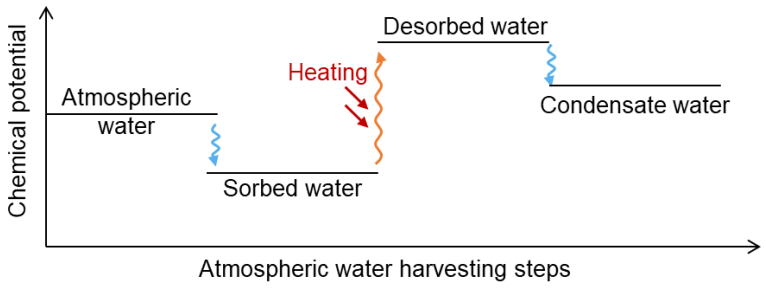

Fig. S2-1. Changes of chemical potential in AWH.

Rapid sorption. Once the cooling is introduced, the chemical potential difference ($\Delta\mu=\mu_{H2O,a}-\mu_{H2O,s}$) between atmospheric water and water in sorbent is enlarged, resulting in the increased driving force for the sorption process. As seen in Fig. 1E, when the ambient condition is at 25°C/60%RH, $\mu_{H2O,a}$ is -238.46 kJ/mol. $\mu_{H2O,s}$ is -239.47 kJ/mol when sorption temperature at 25°C, and corresponding $\Delta\mu$ is 1.0 kJ/mol. Once the cooling is employed, the $\Delta\mu$ increased to 1.56 kJ/mol when the sorption

temperature at 20°C, and then increased to 1.9 kJ/mol at sorption temperature of 17°C. For an arid condition (e.g., 30°C/30%RH), the sorption cannot occur spontaneously due to $\mu_{H2O,a}<\mu_{H2O,s}$. The decreased sorption temperature led to the reduced $\mu_{H2O,s}$, which makes sorption possible. When sorption temperatures are at 21, 18, 15°C, the Δμ are increased to 0.28, 0.61 and 0.95 kJ/mol. The experimental evidence also confirmed the above conclusion, as shown in Fig. 1G. Compared with the control case (without cooling), the time of sorption equilibrium could be shortened within 15 minutes. The linear driving force (LDF) model was used to quantify the sorption dynamics in Fig. S2-2A, showing that decreasing sorption temperature could increase the sorption dynamics.

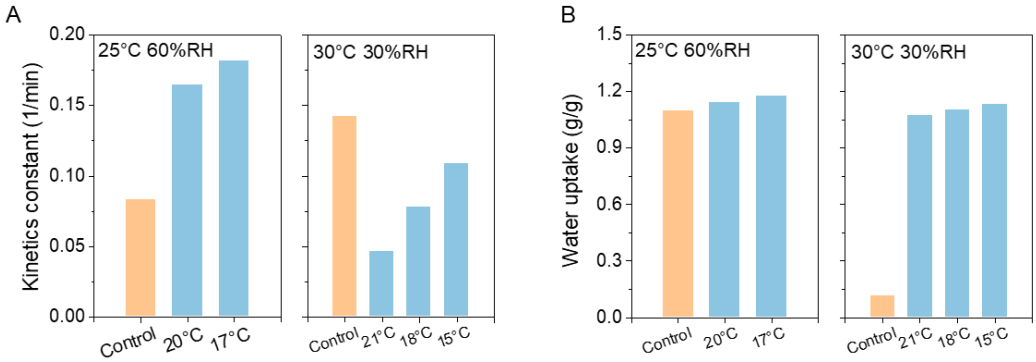

Fig. S2-2. Predicted sorption rate (A) and water uptake (B) under different conditions.

Enhanced capacity. As explained in Fig. 1G, reduced sorption temperature makes the $\Delta\mu$ increase, resulting in enhanced sorption capacity. Indeed, the sorption capacity can be determined by the isotherm. Considering two variables including temperature and humidity, *Polanyi* sorption theory uses the sorption potential (ΔF) to unify the temperature and humidity (Note S1).

Based on the sorption potential, we theoretically calculated the sorption capacity at different conditions, as shown in Fig. S2-2B. The results revealed that the enhancement of sorption capacity at 25°C/60%RH is weaker than that at arid climate with a cooling effect, which is consistent with the experimental results. In summary, the main advantages of using cooling are improved kinetics and enhanced capacity in mild and arid climates, respectively.

Note S3. Mass transfer resistance and linear driving force model

The sorption process can be divided into three main steps, (1) diffusion from external air to sorbents; (2) vapor transport in inter-crystalline pores; (3) sorption reaction within pores inside sorbents, as shown in Fig. S3-1. Each step is driven by the water vapor pressure (or concentration) difference (Δp). The p_{air} and p_{surf} are respective water vapor pressure of ambient air and the surface of sorbents. The p_{sorb}, and p_{sorp} are intra-vapor pressure within sorbent and sorption equilibrium vapor pressure, respectively. Accordingly, the surface diffusion resistance R_{surf} is governed by the mass transfer coefficient, which can be improved by forced air flow; inter-crystalline resistance R_{inter} is determined by the porosity (τ), tortuosity factor (ε), mass transfer thickness (δ) and effective diffusion coefficient, which can be optimized by materials engineering with reduced tortuosity and dimension; intra-crystalline resistance R_{intra} is controlled by sorption reaction coefficient k_e. All these coupled factors determine the sorption dynamics.

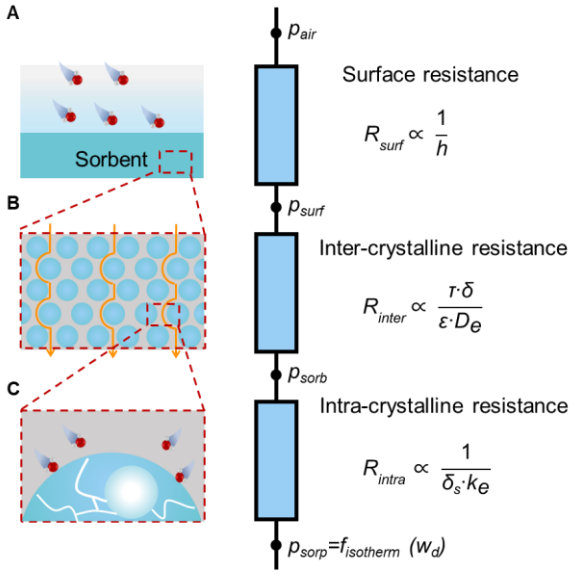

Fig. S3-1. Mass transfer resistance network at the sorption process. (A) External diffusion. (B) Inter-crystalline diffusion. (C) Intra-crystalline diffusion.

In this work, once the sorption temperature is reduced to a sub-ambient temperature, the sorption equilibrium inside the pore is broken and trends to reach the next equilibrium. Considering the reduced (adsorbed water) vapor pressure with decreased temperature within the pore, the water vapor difference between air (free water) and pore of sorbent (absorbed water) is increased (p_{air} - p_{sorp}), contributing to a raised dynamic sorption rate. Besides, the forced convective airflow of external air enhanced the mass transfer coefficient (h), leading to an increased sorption rate. Furthermore, the reduced dimension (δ) with thin coating form (~300 μm) also performs a lower mass transfer resistance compared with the packed sorbent (several centimeters) when scaling up AWH. Therefore, all these contributions enhanced sorption dynamics.

The linear driving force (LDF) model is often used to evaluate the sorption kinetics, which can be described below,

$$\frac{dx}{dt} = k\left(q_{eq} - x\right) \tag{S28}$$

where the x, k and q_{eq} refer to the dynamic water uptake (g), sorption kinetics constant (1/s) and equilibrium capacity (g), respectively.

By integrating the Eq. S28, and assuming that the initial water uptake is zero (x=0, t=0), the Eq. S28 can be expressed as

$$x=q_{eq}\left(1-e^{-kt}\right) \tag{S29}$$

If the normalized water uptake is uniform, Eq. S29 can be expressed as

$$x^{*}=1-e^{-kt} \tag{S30}$$

where x^{*} means the normalized water uptake (-).

The sorption kinetics is determined by the internal and external diffusion. At the micro-scale of sorbents, the internal diffusion is tightly impacted by the pore size and pore environments. Previous works have reamplified pore engineering to enhance the sorption rate. However, for an active AWH, the external diffusion is also crucial for the sorption rate, which is determined by sorbent mass, airflow rate, sorbent structure, etc. For this reason, the direct comparisons between different works are unfair and meaningless. Despite this, the changing trend of the sorption rate coefficient is obvious because the change of sorption rate shows an exponential trend.

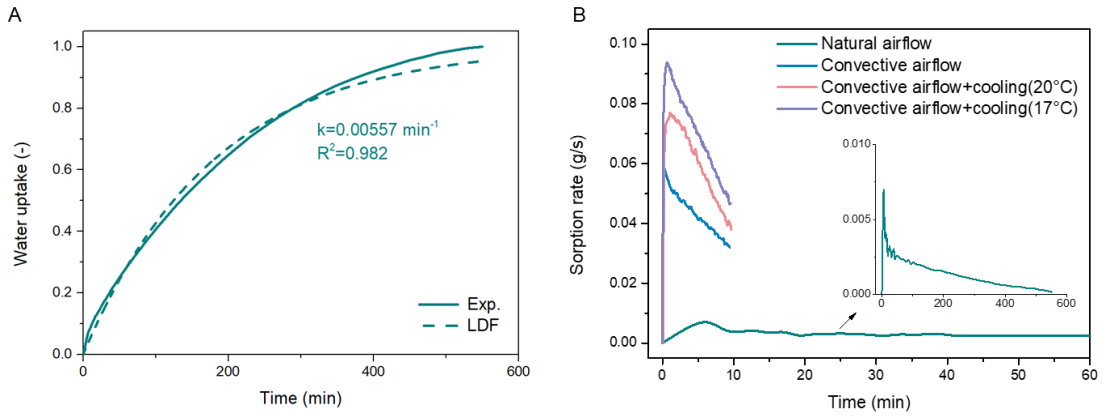

Fig. S3-2. (A) Water sorption dynamics test using MOF adsorber in a natural airflow at 25°C/60%RH. (B) Comparison of sorption rate at 25°C/60%RH.

Effects of convective airflow:

The external airflow influenced the external surface resistance R_{surf}. For the natural airflow (Re<200), the mass transfer coefficient can be calculated by[17]

$$h_m=1.87\times10^{-10}\frac{\frac{T^{2.072}}{P}\left(2.0+0.6Re^{\frac{1}{2}}Sc^{\frac{1}{3}}\right)}{2r} \tag{S31}$$

For the forced convective airflow, the mass transfer coefficient can be calculated based on the Chilton-Colburn analog[18,19],

$$h_m=\frac{h_T D_a}{\lambda_a} \tag{S32}$$

where the heat transfer coefficient h_T can be determined by

$$h_T=j\frac{C_{pa}\rho_a u_a}{Pr^{\frac{2}{3}}} \tag{S33}$$

$$j=0.086Re^{A1}N^{A2}\left(\frac{P_f}{d_c}\right)^{A3}\left(\frac{P_f}{D_h}\right)^{A3}\left(\frac{P_f}{X_t}\right)^{-0.93} \tag{S34}$$

$$A_1 = -0.0361 - \frac{0.042N}{\ln Re} + 0.158 \ln\left(N\left(\frac{P_f}{d_c}\right)^{0.41}\right) \quad \text{(S35)}$$

$$A_2 = -1.224 - \frac{0.076\left(\frac{X_t}{D_h}\right)^{1.42}}{\ln Re} \quad \text{(S36)}$$

$$A_3 = -0.083 - \frac{0.058N}{\ln Re} \quad \text{(S37)}$$

$$A_4 = -5.735 + 1.21 \ln\left(\frac{Re}{N}\right) \quad \text{(S38)}$$

Table S3-1. Parameters for mass transfer calculations

Symbol	Explanation	Value
N	number of tube rows in the air flow direction	2
P_f (m)	fin pitch	0.003
D_c (m)	outer diameter of copper tube	0.00959
D_h (m)	hydraulic diameter	0.00415
X (m)	transverse tube pitch	0.024

Based on the above equations, the mass transfer resistance ($R_{surf}A=1/h_m$) for natural airflow and forced airflow can be determined as 194.63s/m and 24.08s/m, respectively, showing that introducing a convective airflow will reduce this external resistance, which agrees with the results obtained from literature[6]. The difference in external surface resistance explained the mass transfer rate could improve 87.7% by external convective airflow, which agreed with the results obtained from kinetic constant. Fig. S3-3 also shows the changes of external surface resistance with air velocity, indicating that the decrease of $R_{surf}A$ becomes slow with the increase of air velocity.

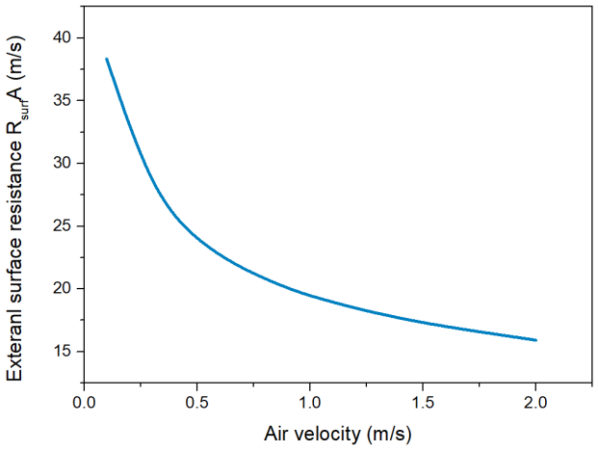

Fig. S3-3. Relationship between surface resistance and air velocity.

Effects of cooling:

For the cooling effects, as shown in Fig. S3-2, the reduction of sorption temperature lowers the water vapor concentration at equilibrium state, thus the driving force for water sorption is increased, which also can be validated from the simulation results in Fig. S6. As shown in Fig. S3-2B and Fig. S21, compared with the control case (sorption at 25°C), applying cooling temperature of 20°C will contribute the 63.3% improvement of sorption kinetics, and 109.8% for sorption at 17°C.

Note S4. Calculations of performance index

The four thermos/hygrometers (HygroFlex3) with an accuracy of ±0.3°C and ±2%RH are used to record the inlet/outlet air temperature and humidity of the adsorber and condenser, as shown in Fig. S16. According to the temperature and humidity, the humidity ratio Y_a can be decided by Eq. S39-S40.

$$Y_a=622\frac{RH\cdot p_{vs}}{101325\text{-}RH\cdot p_{vs}} \tag{S39}$$

$$p_{vs}=\exp\left(\frac{c_0}{T_a}+c_1+c_2T_a+c_3T_a^2+c_4T_a^3+c_5\ln T_a\right) \tag{S40}$$

where the p_{vs} is the saturated vapor pressure at temperature, and the constants are c_0=-5800.2206, c_1=1.3914993, c_2=-0.0048640239, c_3=4.1764768×10^{-5}, c_4=-1.4452093×10^{-8}, c_5=6.5459673.

The adsorbed or released water (m_{ad} or m_{re}) can be calculated based on the area of humidity difference, as shown in Eq. S41-S42.

$$m_{ad}=V_{a,ad}\int_{t_0}^{t}\left(\rho_{a,o,ad}Y_{a,o,ad}\text{-}\rho_{am}Y_{am}\right)dt \tag{S41}$$

$$m_{re}=V_{a,de}\int_{t_0}^{t}\left(\rho_{a,o,de}Y_{a,o,de}\text{-}\rho_{a,in,de}Y_{a,in,de}\right)dt \tag{S42}$$

where the $V_{a,ad}$ and $V_{a,de}$ present the volume flow rate of sorption and desorption air (m^3/s), respectively. The subscripts *a*, *ad*, *de*, *o*, *in* mean the air, adsorption, desorption, outlet and inlet, respectively. Since the density changes with the temperature, the different density at different temperature is considered, which is shown in Eq. S43.

$$\rho=\frac{101325*(1+Y_a)}{287*T_a*(1+1.606*Y_a)} \tag{S43}$$

The release efficiency can be determined as

$$\eta_{re}=\frac{m_{re}}{m_{ad}} \tag{S44}$$

Note S5. Critical cooling and heating temperature

Water sorption isotherms (W_d vs. RH) with different temperatures indicated that the MIL-101 is not sensitive to temperature but humidity (Fig. S3). The operational humidity window (RH_L~RH_H), which refers to the step RH range, is located at the ca. 30-50%RH. To first evaluate the required cooling and heating temperature, it is assumed that the water sorption isotherms (W_d vs. RH) are fixed with different temperatures.

Then, if the ambient humidity is lower than 30%RH, the maximum cooling temperature should allow the sorption by keeping the local humidity near the sorbent higher than 50%RH. Therefore, the relationship between cooling temperature (T_c) and ambient condition (T_{am}, RH_{am}) can be evaluated by

$$\begin{cases} p_{am}=RH_{am}\times p_{vs,am} \\ T_c=T\left(p_{am,}RH_H\right) \end{cases} \tag{S45}$$

where the saturated pressure of water vapor can be calculated by Eq. S40. Since the cooling operation cannot change the water vapor pressure p_{am} (or absolute humidity Y_{am}), the humidity ratio will be constant before and after the cooling operation.

Considering the heat transfer resistance, the temperature of internal fluid should be 2~3°C lower than T_c. During the desorption stage, the closed desorption-to-condensation loop leads to constant water vapor pressure p_{cd} (or absolute humidity Y_{cd}) in the condenser and desorber. Thus, the desorption temperature

is determined by the condensation temperature due to the saturated water vapor in condenser. Assuming that the cooling energy from the adsorber can be recovered to the condensation process, the condensation temperature (T_{cd}) will be 5~10°C higher than the cooling temperature (T_c) considering the temperature difference caused by heat transfer. Therefore, the minimum heating temperature (T_h) can be calculated by

$$\begin{cases} p_{cd}=p_{vs,\ cd} \\ T_h=T\left(p_{cd,}RH_L\right) \end{cases} \quad \text{(S46)}$$

Accordingly, the temperature of internal fluid should be 2~3°C higher than T_h considering the heat transfer resistance.

However, the theoretical critical temperature will be influenced by the practical parameters and sorbent properties. For example, the isotherms will be slightly different at a larger temperature swing, thus making the calculated cooling or heating temperature will be changed. Also, the heat capacity and sorption heat will change the practical sensible and latent heating energy or heat transfer resistance. Despite that, the calculated ideal and critical cooling and heating temperature will give help to the first selection. In addition, because the critical cooling and heating temperature are respective maximum and minimum temperatures, the lower cooling or higher heating temperature is the benefit to higher water production, as revealed in Fig. 2-3.

If the ambient humidity is higher than 50%RH, the humidity itself is in the operational RH range. Thus, the reduced cooling temperature will contribute to the boosted sorption kinetics. In this case, we set the cooling temperature as only 2~3°C lower than the ambient temperature.

Based on the above analysis, to evaluate the minimum potential of water production under different ambient conditions, the related cooling and heating temperatures are calculated based on Eq. S45-S46, as shown in Fig. S24. For 35°C/20%RH and 10°C/40%RH, the cooling and heating temperatures were 17/55°C and 7/38°C, respectively. For 30°C/80%RH and 10°C/80%RH, the cooling and heating temperatures were 26/60°C and 8/38°C, respectively.

Note S6. Cost analysis

We try to evaluate the techno-economics of water supply using our fabricated MOF water harvester. Firstly, we calculated the capital cost (including the cost of the sorbent and device) and operational cost. The calculation of raw materials for sorbent is based on the EXW (Ex Works) from the ECHEMI (https://www.echemi.com/), as listed in Table S5.

Capital cost. The main costs of sorbent are from the consumed solvent during the active periods, occupying 95% of the total costs of sorbent. In this case, developing a facile synthesis method is conducive to reducing the costs of sorbents, especially for MOF. In this work, we loaded 100 g MOF totally in the two same heat exchangers, thus the related costs of MOF are $7.87 USD. It should be noted that the market prices of raw materials depend on the required amounts. If the large-scale AWHs are implemented, the costs of sorbent can be further reduced.

Although the sorbent cost is seemly high, the demonstration of this work validated the water productivity per kg MOF per day can be improved by around one order of magnitude compared reported MOF water harvester. In this case, producing specific water per day (e.g., 4L/d) needs less amount of MOF, resulting in low sorbent cost in a real-applications.

The cost calculations of the device are based on the market price in China. All components are included into the evaluation. As seen in Table S6, the main costs are from the compressor, air fans, valve and condenser. Because purchasing single components from the market is relatively expensive, these costs

may be reduced if a large-scale fabrication is possible. For the fabricated MOF water harvester based on the field test, the total costs of the device are ca. $215.3 USD.

Operation cost. For the operation cost during the running periods of the harvester, according to the field test results, the 2.96 kWh is needed for producing 1L water, a corresponding operating cost of $0.24 USD/L based on the electricity price in China, which is lower than the price of commercial drinking water in China ($0.55-0.97 USD/L). Considering the high-efficiency heat pump can be designed for a large-scale AWH, the power consumption can be reduced to at least one-third of the current power consumption, showing the competitive potential for a commercial dewing harvester (5.6 kWh/L in arid conditions and 2.52 kWh/L in mild conditions)[1].

Based on the above analysis, the payback could be determined as

$$Payback(d) = \frac{C_{cap}}{(P_{water} - C_{op})R} \quad (S47)$$

where C_{cap} ($), C_{op} ($/L), P_{water} ($/L), and R (L/d) refer to the capital cost, operation cost, local water price, and daily water requirement, respectively.

Based on the field test results, a single device could produce 990.4 mL water per day and a mass-based productivity of 9.9 L/kg. Assuming that the minimum amount of water is 4 L/d per person for basic personal survival, and considering the commercial water price is $0.55 USD/L, the predicted payback is 1.97 years (ignoring the depreciation). For humid conditions, the payback could be reduced to 1.36 years.

Supplemental References

1 F. Bagheri, *Water Resources and Industry*, 2018, **20**, 23–28.

2 N. Hanikel, M. S. Prévot, F. Fathieh, E. A. Kapustin, H. Lyu, H. Wang, N. J. Diercks, T. G. Glover and O. M. Yaghi, *ACS Cent. Sci.*, 2019, **5**, 1699–1706.

3 H. A. Almassad, R. I. Abaza, L. Siwwan, B. Al-Maythalony and K. E. Cordova, *Nat Commun*, 2022, **13**, 4873.

4 L. Hua, J. Xu and R. Wang, *Nano Energy*, 2021, **85**, 105977.

5 F. Fathieh, M. J. Kalmutzki, E. A. Kapustin, P. J. Waller, J. Yang and O. M. Yaghi, *Sci. Adv.*, 2018, **4**, eaat3198.

6 J. Xu, T. Li, T. Yan, S. Wu, M. Wu, J. Chao, X. Huo, P. Wang and R. Wang, *Energy Environ. Sci.*, 2021, **14**, 5979–5994.

7 A. LaPotin, Y. Zhong, L. Zhang, L. Zhao, A. Leroy, H. Kim, S. R. Rao and E. N. Wang, *Joule*, 2021, **5**, 166–182.

8 H. Shan, C. Li, Z. Chen, W. Ying, P. Poredoš, Z. Ye, Q. Pan, J. Wang and R. Wang, *Nat Commun*, 2022, **13**, 5406.

9 H. Kim, S. Yang, S. R. Rao, S. Narayanan, E. A. Kapustin, H. Furukawa, A. S. Umans, O. M. Yaghi and E. N. Wang, *Science*, 2017, **356**, 430–434.

10 A. J. Rieth, S. Yang, E. N. Wang and M. Dincă, *ACS Cent. Sci.*, 2017, **3**, 668–672.

11 H. Kim, S. R. Rao, A. LaPotin, S. Lee and E. N. Wang, *International Journal of Heat and Mass Transfer*, 2020, **161**, 120253.

12 O. Labban, T. Chen, A. F. Ghoniem, J. H. Lienhard and L. K. Norford, *Applied Energy*, 2017, **200**, 330–346.

13 H. Kim, S. R. Rao, S. Narayanan, E. A. Kapustin, S. Yang, H. Furukawa, A. S. Umans, O. M. Yaghi and E. N. Wang, *Science*, 2017, **358**, eaao3139.

14 Y. Feng, R. Wang and T. Ge, *Advanced Science*, 2022, **9**, 2204508.

15 Y. H. Feng, Y. J. Dai, R. Z. Wang and T. S. Ge, *Applied Energy*, 2022, **311**, 118732.

16 R. Li and P. Wang, *Nat Water*, 2023, **1**, 573–586.

17 A. Sharafian and M. Bahrami, *International Journal of Heat and Mass Transfer*, 2013, **59**, 262–271.

18 T. Higashi, L. Zhang, M. Saikawa, M. Yamaguchi, C. Dang and E. Hihara, *International Journal of Refrigeration*, 2017, **84**, 228–237.

19 M. Jagirdar and P. S. Lee, *Applied Energy*, 2018, **212**, 401–415.